Climatological and Synoptic Aspects of Intense Arctic Cyclones in the Late Summer

Ian C. Beckley

A Thesis submitted in partial fulfillment of

the requirements for the degree of

Master of Science

(Atmospheric and Oceanic Sciences)

at the

University of Wisconsin-Madison

May 2023

Thesis Declaration and Approval

I, Ian C. Beckley, declare that this Thesis titled 'Climatological and Synoptic Aspects of Intense Arctic Cyclones in the Late Summer' and the work presented in it are my own.

Ian C. Beckley		
Author	Signature	Date

I hereby approve and recommend for acceptance this work in partial fulfillment of the requirements for the degree of Master of Science:

Jonathan E. Martin		
Committee Chair	Signature	Date

Tristan L'Ecuyer		
Faculty Member	Signature	Date

Ángel Adames-Corraliza		
Faculty Member	Signature	Date

Abstract

Climatological and Synoptic Aspects of Intense Arctic Cyclones in the Late Summer

by Ian C. Beckley

A catalog of intense, Arctic cyclones which reached a minimum sea-level pressure of at least 984 hPa was formed for the late-summer months of August and September over the first 15-years of the CloudSat/CALIPSO satellite era, 2006-2020. A subset of events which interacted with Arctic sea-ice was retained for further analysis. During August, intense ice-interacting Arctic cyclones tend to form along the northern coasts of central Eurasia and traverse the eastern Arctic seas before occluding over the remaining Arctic ice sheet. In September, however, such events typically form in the North Atlantic or in the Greenland and Norwegian seas before encountering sea-ice in the waters near Svalbard. Separate four-month composites were made using the stormiest and least stormy Augusts and Septembers over the study period. Composite differencing reveals notable differences in upper-level circulation associated with stormy periods; namely strong, poleward directed upper-level winds along coastal Eurasia (the North Atlantic) during August (September).

An intense Arctic cyclone in August 2010 was observed by CloudSat/CALIPSO during its post-mature phase. The synoptic-dynamic environment and structural characteristics associated with this cyclone were interrogated in detail. This cyclone developed in a region of cyclonic vorticity advection by the thermal wind during the release of baroclinic

instability. The circulation associated with this strong cyclone led to an expansive region of sea-ice rearrangement in which off-ice (on) flow was associated with local gains (losses) in sea-ice concentration. CloudSat/CALIPSO observations across the occluded thermal ridge structure associated with this cyclone indicated that clouds acted to cool the surface adjacent to a region of pronounced sea-ice concentration losses, evidence that the effect of clouds on the sea-ice distribution was small relative to that of the cyclone's circulation.

While the primary effect of the August 2010 cyclone on local sea ice was re-arrangement, an analysis of 6-hr changes in sea-ice area within a domain covering the greater cyclone circulation indicates that an important secondary effect is to modulate the 6-hr sea-ice area change rate relative to climatology. When in its mature phase, the cyclone was coincident with a drastic decline in local sea-ice area and an increase in the magnitude of the 6-hr loss rate. During cyclolysis, however, off-ice flow prevailed throughout the domain and much of the lost ice area was regained. The aggregate of these changes during the storm period was towards sea-ice loss, however, the net effect of this particular intense cyclone is not entirely straight-forward. This motivates further exploration of the topic, particularly with regard to the aggregate effect of multiple cyclones within a month or season.

"Most natural phenomena occurring in the climate system are characterized by great irreversibility and evolve in time with a marked increase in entropy. For example, turbulent motions in the planetary boundary layer do not spontaneously develop into the large-scale organized flow of the general circulation. Neither can a cloud be reconstituted from the same water it lost previously through precipitation. Nor do rivers flow backwards from the sea to their headwaters. Ocean water does not spontaneously decompose into oxygen and hydrogen. None of these phenomena happen naturally in the climate system."

Adapted from Peixoto and Oort (1992)

Dedicated to John Pitz, who taught me that math is the universal language.

Acknowledgements

My parent's dedication to education, whether through home-schooling, tuition or moral support, laid the groundwork for any of my apparent sucesses. My sister, Alexina, first showed me perfectionism and, today, reminds me to carve my own path through life. Dave Irish introduced me to the world of professional sailing and, despite his grueling expectations, allowed me the opportunity to grow beyond amateurism. John and Dottie Pitz have been among my most unfailing supporters. Finally, I must thank my partner, Anna Thickens, as well as the countless life-long friends I have made on my academic journey.

The specific training employed here began with the terrific mentorship of Professors Neil Laird and Nick Metz. Professor Metz first educated me in synoptic meteorology, and Professor Jon Martin carried the burden of exhaustive inquisition into the present day. Lab-mates Patrick, Poush, Libby and Maria have been equally patient during my earlier career. I look forward to watching their individual careers flourish. Thanks to Professor Matt Hitchman, Professor Ángel Adames-Coralliza and Hamish Prince for many stimulating scientific discussions. I have been blessed by dozens of talented educators and peers in a variety of subjects, all of whom have been influential in my development.

This document benefited greatly from the comments of three reviewers: Jon Martin, Tristan L'Ecuyer, and Ángel Adames-Corraliza. Claire Mundi provided Fig. 3.6 and has been dutiful in her sharing of information, data and methods. This research was made possible by National Science Foundation grant # 1951757.

Contents

Abstract **ii**

Dedication **v**

Acknowledgements **vi**

Contents **vii**

List of Figures **ix**

List of Tables **xi**

1 Introduction **1**
1.1 State of Arctic sea ice 1
1.2 Arctic cyclones 3
1.2.1 Interactions with Arctic sea ice 3
1.2.2 Baroclinicity, storm tracks and development 3

2 Catalog of intense Arctic cyclones in late summer **13**
2.1 Arctic cyclone identification 13
2.1.1 Methods 13
2.1.2 The distribution of events in space 14
2.1.3 The distribution of events in time 15
2.2 Upper-level height composites 15
2.2.1 Methods 15
2.2.2 August composites 16
2.2.3 September composites 17
2.3 Ice-interacting cyclones 18
2.3.1 The distribution of ice-interacting events 19
2.4 Discussion 21

3 Development of an intense cyclone and its interaction with sea ice **35**
3.1 The cyclone life-cycle 35

3.1.1 Motivation . . . 35
3.1.2 Methods . . . 36
3.1.3 Results . . . 37
3.1.3.1 Synoptic-dynamic environment . . . 37
3.1.3.2 Satellite observations . . . 39
3.2 Arctic sea ice . . . 40
3.2.1 Methods . . . 40
3.2.2 Results . . . 42
3.2.2.1 Local changes in sea-ice concentration . . . 42
3.2.2.2 Sea-ice area . . . 43
3.3 Discussion . . . 45

4 Summary, conclusions and recommendations for future work 55
4.1 Climatology of intense, Arctic cyclones in late summer . . . 55
4.2 Synoptic analysis of an intense, ice-interacting Arctic cyclone . . . 57
4.3 Recommendations for future work . . . 59

A Methods for figures in Chapter 1 61
A.1 Fig. 1.1 . . . 61
A.2 Fig. 1.2 . . . 61
A.3 Fig. 1.3 . . . 62
A.4 Fig. 1.4 . . . 62
A.5 Fig. 1.5 . . . 62

Bibliography 64

List of Figures

1.1 Satellite-era Arctic sea-ice area 8
1.2 Losses in sea-ice area since the mid-2000s 9
1.3 The September sea-ice age distribution since 1984 10
1.4 The mean distribution of August sea-ice variability 11
1.5 August-mean distribution of wind speed and baroclinic growth rates at 500 hPa 12

2.1 Intense August and September Arctic cyclones, 2006-2020 26
2.2 Storm tracks during the stormiest late-summer months from 2006-2020 . 27
2.3 Storm tracks during the least stormy late-summer months from 2006-2020 27
2.4 Standardized 500 hPa geopotential height anomalies for stormy and quiescent Augusts 28
2.5 Standardized 500 hPa geopotential height anomalies for stormy and quiescent Septembers 28
2.6 Difference between stormy and quiescent August upper-level height anomalies 29
2.7 Difference between stormy and quiescent September upper-level height anomalies 30
2.8 An intense Arctic cyclone which interacted with sea-ice, 16 August 2010 . 31
2.9 Ice-interacting, intense August and September Arctic cyclones, 2006-2020 32
2.10 Ice-interacting, intense Arctic cyclones during August and September, 2006-2020 in half month periods 33
2.11 Map of Arctic sea delineations 34

3.1 Daily synoptic, visible satellite, and sea-ice change analysis on 00Z 14 August 2010 48
3.2 As in Fig. 3.1 but for 00Z 15 August 2010 48
3.3 As in Fig. 3.1 but for 00Z 16 August 2010 49
3.4 As in Fig. 3.1 but for 00Z 17 August 2010 49
3.5 Cross-section through an intense, ice-interacting Arctic cyclone at 00Z 16 August 2010 50
3.6 Cloud phase, cloud radiative effect and precipitation type for a cross-section through an intense, ice-interacting Arctic cyclone at 00Z 17 August 2010 51

3.7 A comparison between domains for analysis of sea-ice area 52
3.8 Daily sea-ice concentration analysis for an intense, mid-August Arctic cyclone in the Barents Sea 53
3.9 Analysis of sea-ice area and its change in the vicinity of the mid-August 2010 cyclone 54

List of Tables

2.1 Cyclone counts and basic statistics: all intense Arctic cyclones 24
2.2 Cyclone counts and basic statistics: intense, ice-interacting cyclones . . . 25
2.3 Intense, ice-interacting Arctic cyclones from 2006-2020 for each Arctic sea 25

Chapter 1

Introduction

1.1 State of Arctic sea ice

The Arctic climate has undergone substantial changes since the early 20th century, perhaps chief among them a drastic decline in total sea-ice area. This trend has accelerated into the 21st century, so much so that the mean sea-ice area in the 2010s was approximately one standard deviation below the 1979-2021 climatology (Fig. 1.1). This is a shocking departure from the 1980s distribution, and is associated with substantial losses of summer-time sea-ice area since the mid-2000s, especially in the Kara, Laptev and Beaufort Seas (Fig. 1.2). The deterioration of the Arctic ice sheet decreases local albedo and, under clear-sky conditions, increases the absorption of solar insolation. This ice-albedo feedback mechanism has the potential to accelerate ice loss, especially in the summertime, and contributes to the increasing fragility of the Arctic ice sheet.

In addition to losses in total sea-ice area, status quo ice-age characteristics have been recently upended. In the late 1980s, nearly half of the prevailing September ice sheet was composed of resilient, 4+ year-old ice (Fig. 1.3). Over time, however, the ice sheet has become increasingly characterized by younger, 1-2 year-old ice, especially since the mid-2000s. In 2019, less than 10% of the September ice sheet had persisted for over 3 years, a satellite-era record. Young ice is typically thinner and physically weaker than multi-year ice, especially when at warmer temperatures (Asplin et al., 2012). Indeed, in an analysis of the dramatic retreat of Arctic ice in summer of 2007, Zhang et al. (2008a,b) determined that contemporary sea-ice distributions are increasingly vulnerable to atmospheric forcing.

While the long-term trend in Arctic sea-ice goes quasi-linearly with increasing temperatures (Box et al., 2019), it is thought that non-linearities introduced by the ice-albedo feedback and increasing fragility led to accelerated ice-loss in the mid-2000s (Zhang et al., 2008a,b). This continues to reinforce a lengthened Arctic melt season (Markus et al., 2009), and, even with the IPCC's AR4, "business as usual", greenhouse gas loading scenario, minimum September sea-ice extents are being realized nearly 30 years ahead of ensemble mean model forecasts (IPCC, 2022, Stroeve et al., 2007). The degree to which models may continue to under-predict losses is still subject to robust discussion (e.g. Boé et al., 2009, Stroeve et al., 2007, Wang and Overland, 2009), and no consensus has been reached regarding exactly *how* Arctic sea-ice will meet its demise, let alone when. Further evaluation of this problem still requires detailed analysis of atmospheric and cryospheric observations on short timescales. For example, the effect of extreme precipitation events

and localized cloud-radiative feed-backs remain poorly understood in the sparsely observed Arctic region (Box et al., 2019).

1.2 Arctic cyclones

1.2.1 Interactions with Arctic sea ice

An investigation by Zhang et al. (2013) indicated that extreme precipitation, moisture and heat transport events all occurred nearly simultaneously in the Eurasian Arctic and were predominantly associated with high latitude extra-tropical cyclones. Clancy et al. (2022) demonstrated that intense cyclone events which reached high latitudes typically resulted in a rapid rearrangement of the local ice shelf. Given that the vast majority of sea-ice concentration variability occurs along the ice edge (Fig. 1.4), Arctic cyclones are of primary interest in understanding high-frequency cryosphere/atmosphere interactions. Investigations by Simmonds and Keay (2009) suggest that, in general, stronger and larger storms are associated with a net decrease in sea-ice extent. The preconditioning of ice into a more vulnerable state via prior storms, however, appears to be a complicating factor. For example, Asplin et al. (2012) demonstrated that the swell associated with even a meager cyclone can produce leads hundreds of kilometers into the ice shelf.

1.2.2 Baroclinicity, storm tracks and development

The Arctic climate has warmed 3°C since 1971, nearly twice that observed over the greater Northern Hemisphere (Box et al., 2019). This is consistent with changes in the

basic state baroclinicity and suggests the possibility of an existing ice-cyclone feedback. Simmonds and Keay (2009) employed the University of Melbourne's cyclone tracking algorithm in an interrogation of changing storm behavior during the satellite era. They reported insignificant increases in cyclone frequency, however, a similar study by Simmonds et al. (2008) reported an increase in the number of intense storms in several prominent reanalysis datasets. These changes were most notable in the summer-time, particularly in the Barents and Kara seas, an indication that the Arctic storm tracks are asymmetric about the hemisphere and the calendar.

The relationship between intense cyclones and baroclinicity was perhaps first noted within the context of the Norwegian cyclone model developed by Bjerknes and Solberg (1922). They described the extra-tropical cyclone as a manifestation of instability along the polar frontal surface. The theoretical understanding of this phenomena developed rapidly in the 1940s with Charney (1947) and Eady (1949) each applying the so-called quasi-geostrophic equations in simplified models. Assuming an f-plane and constant stratification, they demonstrated that the growth rate of unstable disturbances depends linearly on the vertical shear of the geostrophic wind. The thermal wind relation, $\frac{\partial \vec{V}}{\partial p} = \left(\frac{g}{fT}\right) \hat{k} \times \nabla T$ indicates an equivalent statement can be made with respect to the baroclinicity (i.e. the horizontal temperature contrast).

Hoskins and Valdes (1990) approximated the baroclinic growth rate of the most unstable waves as

$$\sigma \approx .31 \times f \left| \frac{\partial \vec{V}_g}{\partial z} \right| N^{-1} \tag{1.1}$$

where f is the Coriolis parameter, $\vec{V}$ is the horizontal wind and N is the Brunt-Vaisala frequency defined as $N = \left(-\frac{g^2 \rho}{\theta} \frac{\partial \theta}{\partial p} \right)^{\frac{1}{2}}$, a measure of stratification. Substituting thermal wind balance into the RHS yields

$$\sigma \approx .31 \times \frac{g}{T} \left| \nabla T \right| N^{-1} \tag{1.2}$$

indicating that the primary extra-tropical storm tracks are located in regions of both strong upper-level winds and strong baroclinicity. The August-mean distribution of 500 hPa winds and baroclinic growth rates are compared using the 1.25° Japanese 55-year Reanalysis (JRA55, Fig. 1.5). Considering only Fig. 1.5a, primary August storm tracks appear in regions characterized by strong upper-level winds, namely the central Pacific and North Atlantic. These regions are additionally characterized by relatively large baroclinic growth rates (Fig. 1.5b). The latter analysis is strongly influenced by topography as demonstrated by the patch of high baroclinic growth rates near the Tibetan Plateau. Similar methodology was employed by Hoskins and Valdes (1990) in their interrogation of Northern Hemispheric, primarily winter-time, storm tracks.

Simultaneous to the theoretical approaches of Eady and Charney, Sutcliffe (1947) interrogated the development of surface pressure systems from the quasi-geostrophic perspective. He demonstrated that the net column divergence was proportional to the advection of geostrophic absolute vorticity by the thermal wind. Since the pressure at the surface corresponds to the weight of the overlying atmospheric column, a net change in mass within the atmospheric column is consistent with a change in the surface pressure. Recalling that the Northern Hemispheric thermal wind blows along temperature contours with cold air to its left (via the thermal wind relation), one can approximately forecast the development of surface disturbances using only maps of 1000-500 hPa thickness (a measure of temperature), 500 hPa geostrophic absolute vorticity and sea-level pressure.

The former analysis of August-mean winds and baroclinic growth rates demonstrates that summer cyclones will be most common in middle-latitudes from around 35-65N. This is not to say, however, that high-latitude cyclones are necessarily physically distinct from their mid-latitude counterparts. Several authors have taken this perspective (e.g. Tanaka et al., 2012), perhaps to the detriment of our understanding of high-latitude cyclones as dynamic phenomena with characteristic baroclinic life-cycles (e.g. Palmén and Newton, 1969, see their Chapter 11). Indeed, recent investigations of Arctic cyclones, especially the intense variety, indicate that these events develop under baroclinic conditions. It follows that their development, synoptic-dynamic environment and structural characteristics may be considered via the aformentioned synoptic charts and the Sutcliffe development theorem (Sutcliffe, 1947). That said, surprisingly few analyses of individual, intense Arctic cyclones employ this simple diagnostic relation (e.g. Simmonds and Rudeva, 2012,

Yamagami et al., 2017). The disjunction between the analytical approaches of classically trained synoptic-dynamicists and the modern interest in Arctic cyclones (especially with regard to their interaction with sea ice) leaves such events unnecessarily shrouded in mystery.

In order to uncover some of this apparent mystery, this thesis employs a traditional synoptic-dynamic analytical approach in an investigation of intense Arctic cyclones and their interaction with sea ice. Chapter 2 describes a 15-year climatology of these events in the late-summer months of August and September. The resulting catalog of intense Arctic cyclones coincides with the first 15-years of the CloudSat/CALIPSO mission, 2006-2020, indicating that detailed observations of the precipitation distribution and radiative effect of clouds exist for some cases. A subset of cyclones which interacted with Arctic sea ice is isolated for further analysis. Additionally included in Chapter 2 is a composite analysis of the upper-level circulation in particularly stormy months.

Chapter 3 includes an analysis of an individual intense Arctic cyclone which interacted with Arctic sea ice in August 2010. The development of this cyclone is described using classical synoptic charts and through the perspective of the Sutcliffe development theorem. This cyclone was observed during its post-mature phase, CloudSat/CALIPSO providing observations across its occluded thermal ridge structure and the associated cloud-head. In addition, discussion is held regarding the effect of clouds and winds associated with this cyclone on the local sea-ice distribution. This thesis concludes with a summary discussion and several recommendations for continued research on this topic.

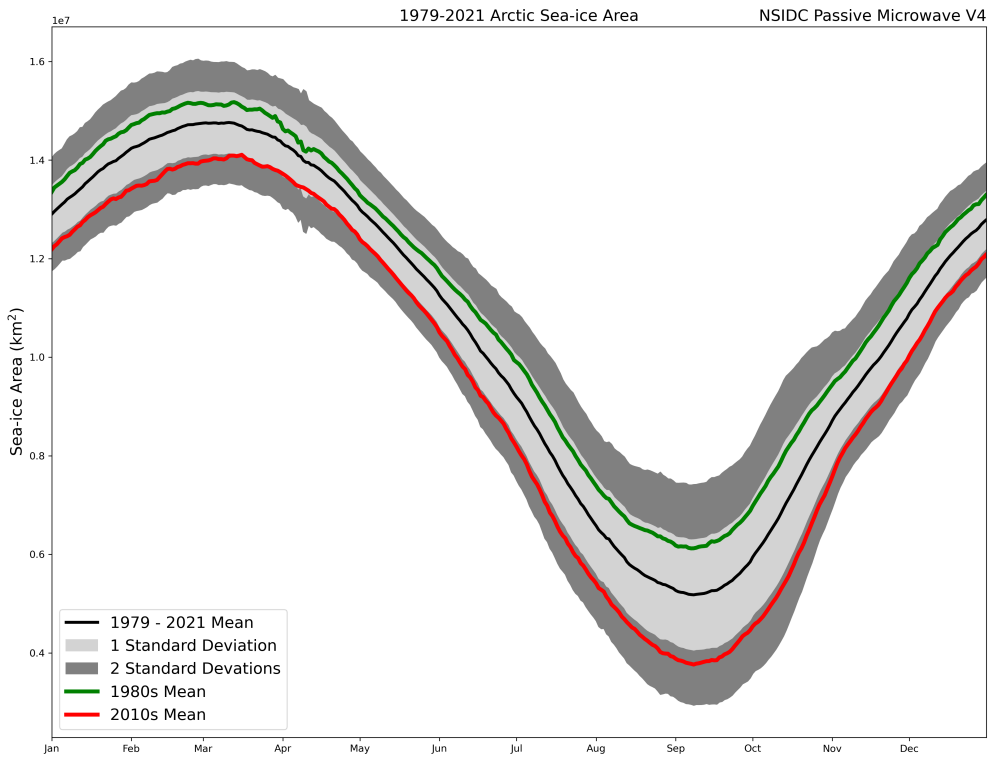

FIGURE 1.1: The climatological sea-ice area for each day of the year over the satellite-era

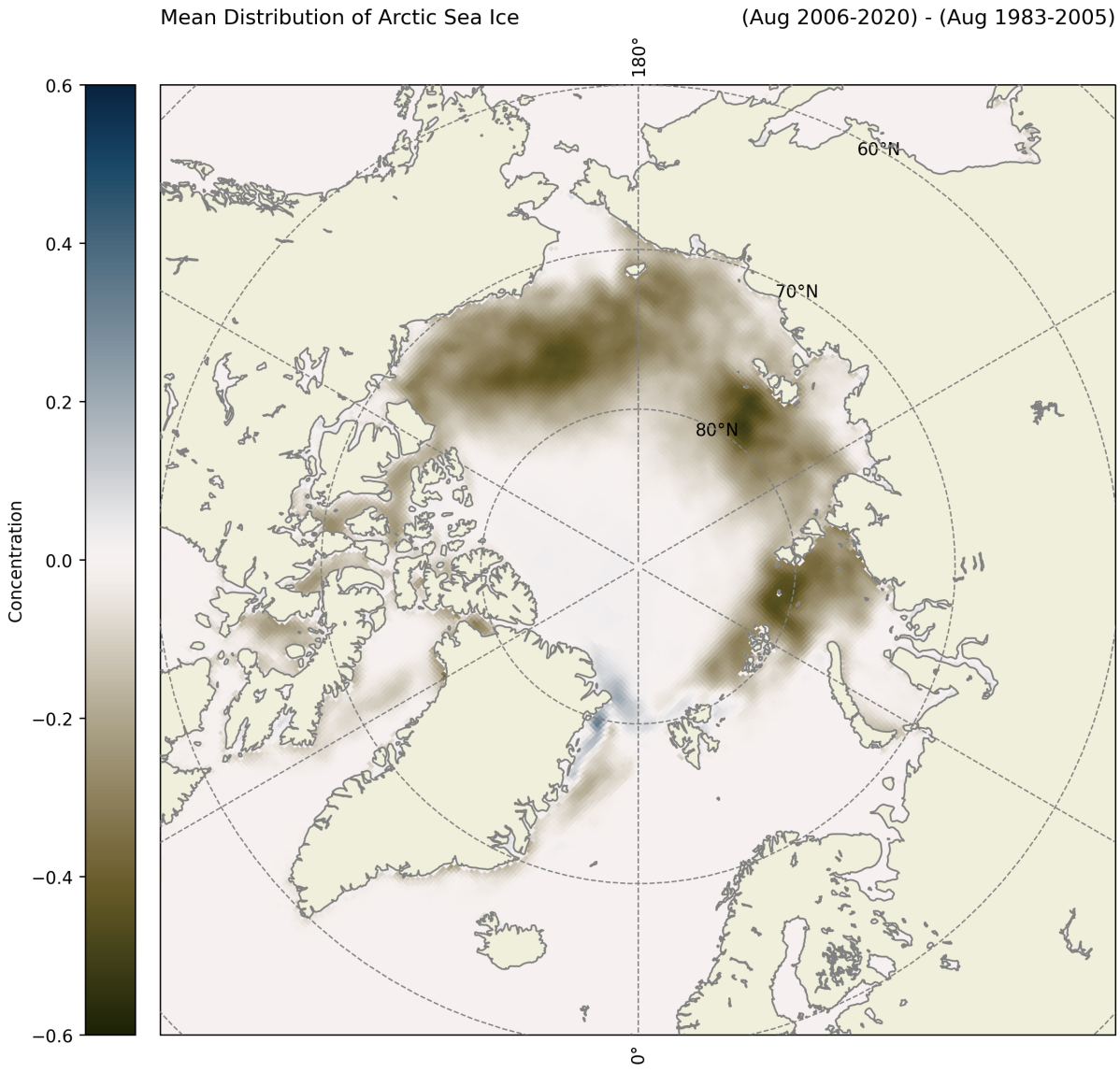

FIGURE 1.2: The difference between the 2006-2020 and 1979-2005 mean sea-ice distributions.

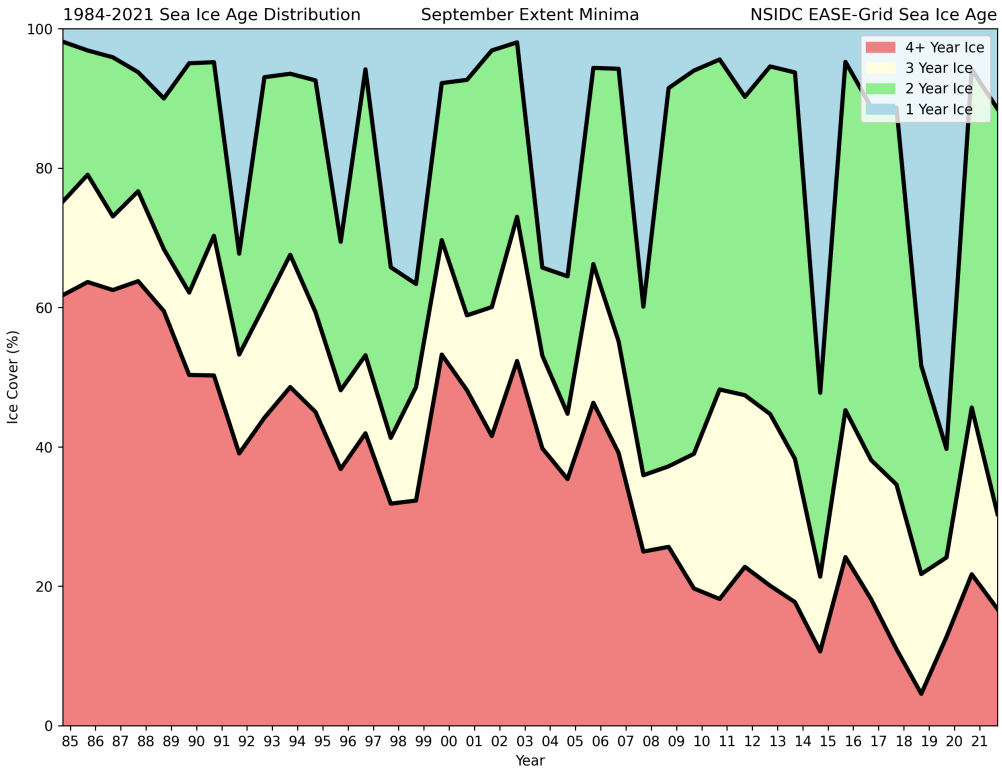

FIGURE 1.3: The sea-ice age distribution during the week of the September sea-ice area minimum since 1984

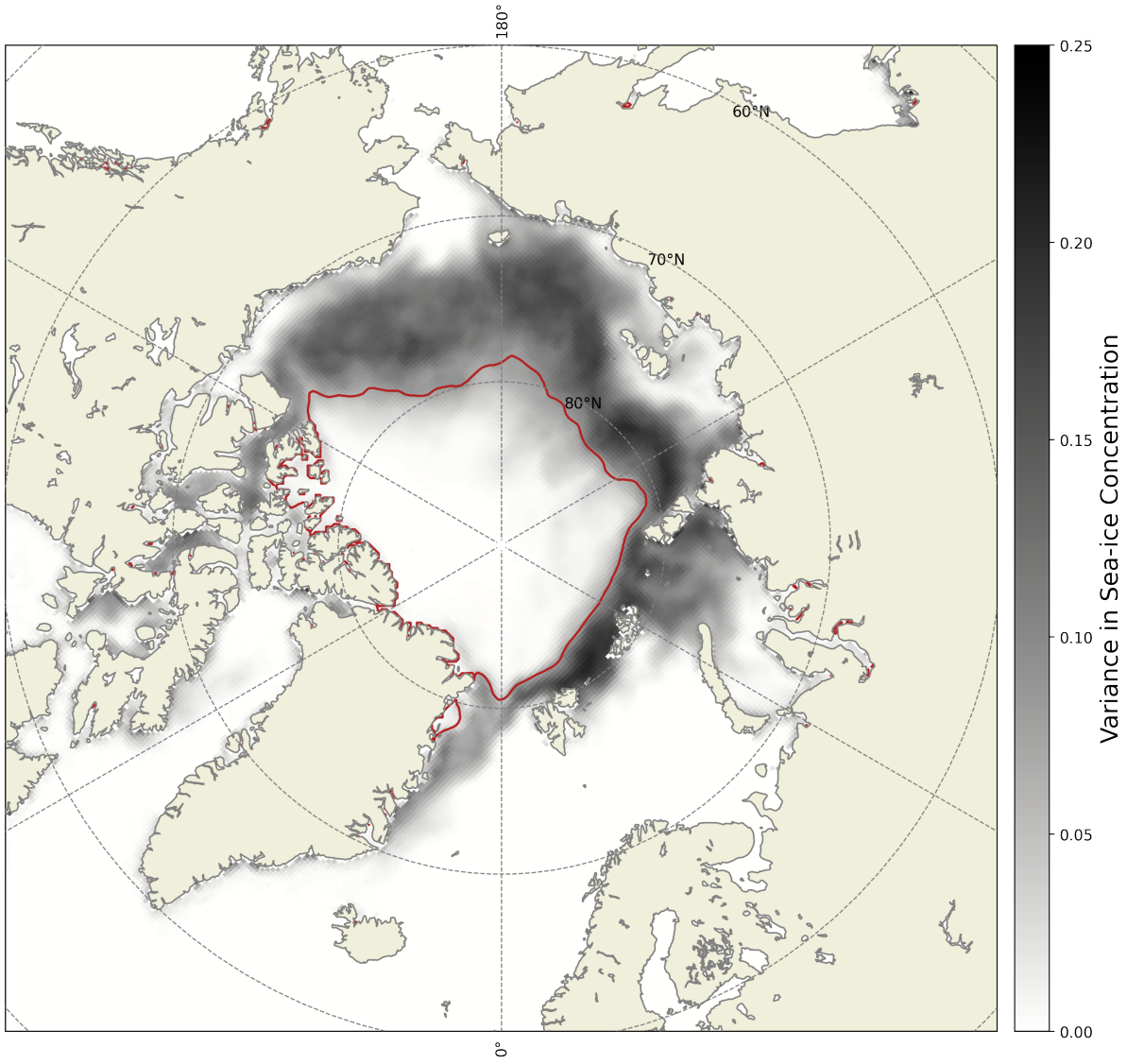

FIGURE 1.4: The mean distribution of August sea-ice variability (black colormesh) from 2006-2020. The red contour corresponds to the August mean 0.8 sea-ice concentration contour from 2006-2020.

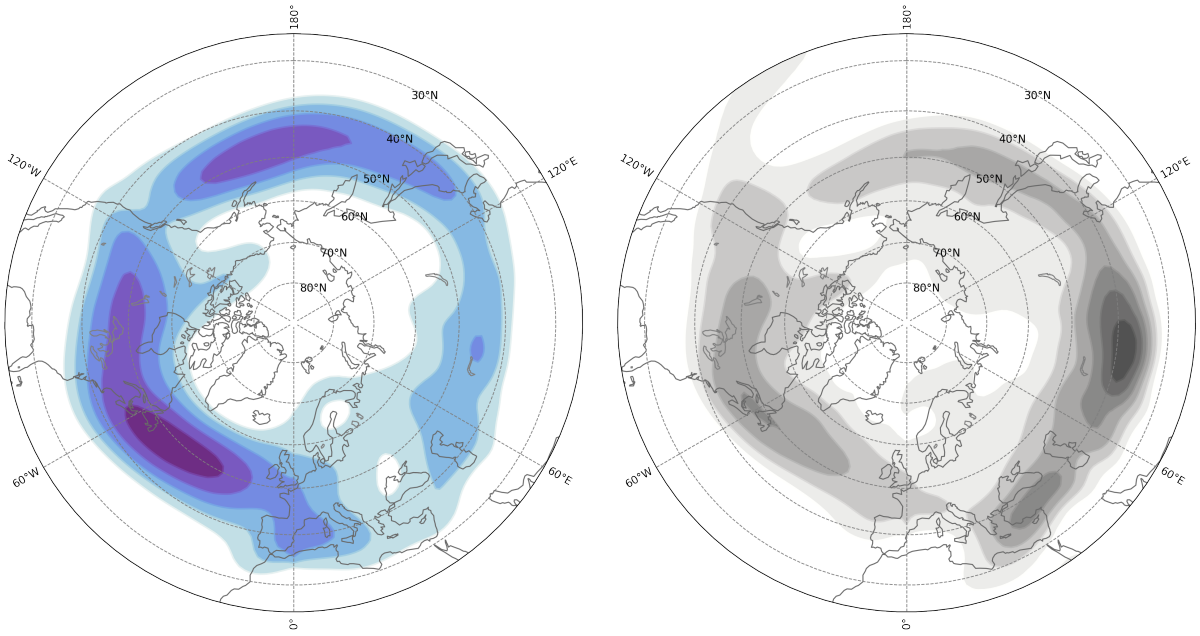

FIGURE 1.5: a.) August-mean wind speed in the JRA55 at 500 hPa contoured from 6 to 18 ms^{-1} every 2 ms^{-1}. b.) as in a.) except for an approximate baroclinic growth rate contoured from 3×10^6 to 11×10^6 s^{-1} every 1×10^6 s^{-1}.

Chapter 2

Catalog of intense Arctic cyclones in late summer

2.1 Arctic cyclone identification

2.1.1 Methods

A catalog of intense, August/September Arctic cyclones was created to cover the early CloudSat/CALIPSO-era, 2006-2020. Events during this period were available for observation by the satellite pair, possibly affording insights into the precipitation distribution and cloud-radiative effect associated with such storms in the ordinarily observation-sparse Arctic. The Japanese 55-year Reanalysis (JRA55, Kobayashi et al., 2015), at 6-hr temporal and 1.25° spatial resolution, provided adequate resolution for both identification and

subsequent analysis of these synoptic-scale features. SLP is routinely contoured every 4 hPa and intense Arctic cyclones were considered those which attained a closed 984 hPa isobar at some point during their life-cycles while poleward of 60N. A similar catalog of August Arctic cyclones produced by Simmonds and Rudeva (2012) indicates that the 984 hPa intensity threshold lies well on the tail of their observed distribution (their Fig. 4a). Individual cyclones were identified semi-objectively on 6-hr sea-level pressure analyses and tracked throughout the interval beginning with the appearance of the first closed 1000 hPa isobar and extending until that feature disappeared. This methodology was successful in identifying over 150 intense Arctic cyclones during the study period. Annual counts and basic statistics associated with these events are tabulated in Table 2.1. Individual storm tracks for all intense Arctic cyclones are provided in Fig. 2.1.

2.1.2 The distribution of events in space

The distribution of all intense, late-summer Arctic cyclones from 2006-2020 reveals the strong influence of the North American and North Atlantic storm tracks (Fig. 2.1a). The vast majority of North American originating events remain between 60-70N, however, there is a tendency for some events originating in the North Atlantic to intensify over the Greenland and Norwegian Seas. A second, substantial portion of high-latitude events originate over northern Eurasia before crossing the Barents, Kara, Laptev and even Siberian Seas. The Chukchi and Beaufort Seas appear relatively devoid of events, the majority of north Pacific originating cyclones dissapating before reaching 70N.

2.1.3 The distribution of events in time

Table 2.1 indicates that the number of intense, late-summer Arctic cyclones varies (sometimes substantially) year to year. Take, for instance, August and September 2016, the stormiest of their respective months with 7 and 10 intense Arctic cyclones, respectively (Fig. 2.2). These active months were particularly emblematic of the preponderance of cyclones having originated in Northern Eurasia and the North Atlantic (Fig. 2.2). Compare that with August 2015 and September 2012 which featured only one and three Arctic cyclones, respectively (Fig. 2.3). Given the relationship between intense cyclones, strongly sheared environments and upper-level vorticity (see Chapter 1), it is reasonable to ask whether clear differences in upper-level circulation arise between stormy and quiescent periods.

2.2 Upper-level height composites

2.2.1 Methods

In order to examine characteristics of the upper-level circulation associated with stormy and quiescent periods, August and September months from 2006-2020 were ranked separately by the number of intense Arctic cyclones which occurred. The four August months with the most (least) number of storms were considered stormy (quiescent). Four-month stormy and quiescent composites of standardized 500 hPa geopotential height anomalies were formed using the 1.25° JRA55 separately for August and September (Fig. 2.4 & Fig. 2.5, respectively). Subtracting a quiescent composite from its stormy counterpart

reveals differences in upper-level circulation between these disparate groups (e.g. Fig. 2.6 & Fig. 2.7).

2.2.2 August composites

In the stormy August composite (Fig. 2.4a), low geopotential height anomalies (troughing) are observed centered over the Norwegian and northern Barents Sea. High geopotential height anomalies (ridging) are observed across Eurasia and over west-central Europe. This is consistent with a westerly geostrophic wind anomaly along coastal Eurasia. This region of enhanced upper-level geostrophic winds is favorable for cyclone development and will be referred to as the Eurasian Arctic storm track. In addition, a northerly geostrophic wind anomaly exists over the Greenland Sea associated with ridging over the eastern Canadian Archipelago. Such a configuration could provide an outlet for tropopause polar vortex (TPV) features to exit high latitudes, round the base of the Norwegian sea trough, and eventually facilitate the development of surface cyclones along the coast of northern Eurasia.

The quiescent August composite describes a markedly different scenario (Fig. 2.4b). For instance, anomalous ridging in the Labrador Sea and troughing over England is consistent with a northeasterly geostrophic wind anomaly in the North Atlantic. Another ridging center over the pole lies adjacent to troughing over coastal Eurasia resulting in an easterly geostrophic wind anomaly in the eastern Arctic. Such a situation is unfavorable for cyclone development in both the North Atlantic and along northern Eurasia, the two primary Arctic storm tracks.

Subtracting the August quiescent composite (Fig. 2.4b) from its stormy counterpart (Fig. 2.4a) emphasizes those features possibly associated with periods of enhanced cyclone development (Fig. 2.6). Generally, stormy Augusts in the Arctic feature anomalously low geopotential heights immediately over the pole, into the Barents and Norwegian Seas and in the North Atlantic. A belt of westerly geostrophic wind anomalies are found along northern Eurasia and into the eastern Arctic seas. Another region of westerly geostrophic wind anomalies are found over the northern Canadian Archipelago and Greenland, potentially directing TPV features towards the Greenland and Norwegian Seas. Such conditions are favorable for cyclone development in the North Atlantic, and, especially along coastal Eurasia.

2.2.3 September composites

The stormiest September months are associated with troughing just north of the Canadian Archipelago extending southward across western Greenland into the North Atlantic (Fig. 2.5a). This departs substantially from the August composite in that the anomalous geostrophic wind is calm over coastal Eurasia. Rather, poleward-directed geostrophic wind anomalies extend from the North Atlantic, along the east coast of Greenland and northward to the pole. This situation is favorable for cyclone development in the North Atlantic, and Greenland and Norwegian Seas.

Quiescent September months are associated with ridging over high latitudes and troughing in the Norwegian Sea (Fig. 2.5b). The upper-level geostrophic wind anomaly in the northern Greenland and Norwegian Seas is easterly, against the westerly mean flow. This

is indicative of relatively weak upper-level flow in the Greenland and Norwegian Seas, a situation unfavorable for cyclone development. A region of northwesterly geostrophic wind anomalies in the North Atlantic near 60N suggests that quiescent September months in the Arctic are associated with a reorientation of the North Atlantic storm track away from the pole relative to stormy years. Again, this quiescent composite departs substantially from its August counterpart (Fig. 2.4b), confirmation that these two late-summer months should be considered separately.

Subtracting the quiescent September composite (Fig. 2.5b) from its stormy counterpart (Fig. 2.5a) demonstrates the influence of strongly anomalous troughing/ridging over the North Atlantic/ Scandinavia (Fig. 2.7). The resulting, poleward-directed geostrophic wind anomaly over the Norwegian and Greenland Seas is favorable for northeastward storm motion from the North Atlantic into the Arctic Ocean. Comparing the September composite difference field (Fig. 2.7) from its August counterpart (Fig. 2.6) reinforces the need to treat these months separately. While stormy Septembers are associated with an enhanced, poleward-directed North Atlantic storm track extending into the Greenland and Norwegian Seas, stormy Augusts feature an invigorated Eurasian storm track.

2.3 Ice-interacting cyclones

In order to isolate events featuring robust sea-ice interactions, gridded sea-ice concentration data from the National Snow and Ice Data Center (DiGirolamo et al., 2022) with daily temporal and 25-km spatial resolution was incorporated into daily synoptic charts

featuring SLP, 1000-500 hPa thickness and daily sea-ice concentration change. For example, Fig. 2.8 depicts an intense Arctic cyclone in the Barents Sea at 00Z 16 Aug 2020. Note the pronounced dipole in daily sea-ice concentration change coincident with the northern periphery of the surface cyclone. Analysis of other cyclones indicated this was the first-order signature of a robust sea-ice interaction. A similar result was presented by Clancy et al. (2022, see their Fig. 7a) in their comprehensive analysis of Arctic cyclones. The appearance of this signature provided a simple delineation between those storms which did and did not robustly interact with the ice sheet resulting in a 73-member subset. Annual counts and basic statistics associated with these events are tabulated in Table 2.2. Individual storm tracks for all ice-interacting, intense Arctic cyclones are provided in Fig. 2.9.

2.3.1 The distribution of ice-interacting events

Upon isolating those events which featured robust sea-ice interactions (Fig. 2.9), it becomes clear that North American-originating, intense cyclones very rarely go on to interact with sea-ice (i.e. compare Fig. 2.1 to Fig. 2.9). Rather, the vast majority of ice-interacting events spawn in the North Atlantic or the Eurasian subcontinent (Fig. 2.9), evidence of a notable asymmetry about the hemisphere. Ranking individual August and September months by annual count in both Table 2.1 and Table 2.2 produces a remarkably similar hierarchy such that qualitative conclusions drawn from Fig. 2.4 & Fig. 2.5 would be essentially unchanged if constructed with respect to the number of

ice-interacting cyclones (rather than all Arctic cyclones). A composite of the four stormiest Augusts (Fig. 2.4a) suggests that stormy Augusts are typically associated with an enhanced storm track predominantly along coastal Eurasia. This contrasts with stormy Septembers which were associated with a poleward-oriented North Atlantic storm track (Fig. 2.5). Given this disparity, it is likely that the distribution of intense, ice-interacting cyclones is strongly dependent on the time of year.

In order to demonstrate this temporal dependence, storm tracks of intense, ice-interacting cyclones were isolated in 15-day periods from early August through late September (Fig. 2.10). No intense, ice-interating cyclones occured in the North Atlantic, Greenland or Norwegian Seas during early August. Instead, all such storms formed along coastal Eurasia and passed through the eastern Arctic seas before interacting with sea ice. The number of events which occured in each Arctic sea (using ocean boundaries defined by the International Hydrographic Organization, available online at http://www.marineregions.org/, see Fig. 2.11) is tabulated in Table 2.3. Despite having the fewest ice-interacting events (Fig. 2.10a), early August featured six events in the Kara Sea alone, the most of any 15 day period (Table 2.3).

Intense, ice-interacting cyclones became increasingly common between early August (N_i = 12) and early September (N_i = 18, Fig. 2.10). Perhaps more remarkable is the westward shift of the event distribution from coastal Eurasia towards Greenland. For example, there were only two events in the Greenland Sea in late August (Fig. 2.10b), up from none earlier that month (Fig. 2.10a). Early September, however, featured five events in the Greenland

Sea (Fig. 2.10c). Eight events were observed there later that month (Fig. 2.10d). A similar increase in event frequency with time was observed in the neighboring Norwegian Sea (Table 2.3). This behavior indicates a transition between the two disparate storm tracks identified in Section 2.2. Whereas stormy Augusts are associated with an enhanced Eurasian storm track, a poleward-directed North Atlantic storm track during stormy Septembers steers intense storms through the Greenland, Norwegian and Barents Seas.

The asymmetrical distribution of intense Arctic cyclones observed in Fig. 2.1 is mirrored within the ice-interacting subset (Fig. 2.9). In fact, the entire 15-year climatology contains only a handful of outliers; three events originating in the Gulf of Alaska and two in the Canadian Archipelago. The Eurasian and North Atlantic storm tracks dominate the distribution of ice-interacting events despite the existence of distinct storm tracks in the central Pacific and central United States, even in August (see Fig. 1.5). Evidently events spawned in those mid-latitude storm tacks very rarely go on to interact with Arctic sea ice.

2.4 Discussion

The tracks of all intense, Arctic cyclones during the study period closely mirror the well-known North American and North Atlantic storm tracks (Chang and Orlanski, 1993, Hoskins and Valdes, 1990, Reitan, 1974). While a substantial portion of all intense, August and September Arctic cyclones develop over North America, comparison between Fig. 2.1 and Fig. 2.9 indicates that rarely do those storms move poleward of 70N. Rather,

two main pathways emerge for intense cyclones to reach high latitudes in the late-summer: one in which cyclones originate in the North Atlantic and develop through the Greenland and Norwegian Seas, and another wherein cyclones originate over northern Eurasia and develop over the Barents, Kara and Laptev Seas. These two regions are the primary Arctic storm tracks during late summer.

While storms can occur in both the Eurasian and North Atlantic Arctic storm tracks regardless of month (e.g. Fig. 2.2), August (September) features a preponderance of events in coastal Eurasia (the North Atlantic). Composite analysis uncovers the influence of upper-level height anomalies on the locations of these storm tracks. In Fig. 2.6, note that the geostrophic wind anomaly blows from the North Atlantic, over Scandinavia and the Barents Sea before turning poleward over the Chukchi Sea. This aligns well with the observed August cyclone distribution (Fig. 2.10a-b) and is consistent with an active Eurasian storm track. Conversely, Fig. 2.7 indicates anomalous upper-level flow directed poleward over the North Atlantic and into the Greenland and Norwegian Seas and along the Eastern Arctic Ocean. This aligns well with the observed September cyclone distribution (Fig. 2.10c-d) and is consistent with an active North Atlantic storm track.

Concerning the paths of ice-interacting cyclones, the vast majority of observed events moved northeastward (poleward and westward) during their development (post-mature) phase. This behavior is not dissimilar to that of mid-latitude cyclones whose development and paths are determined by baroclinic processes (Martin, 2006). Indeed, a primary conclusion of the comprehensive analysis of Arctic cyclones by Clancy et al. (2022) is that

the majority of *intense* Arctic cyclones exhibit robust baroclinic structures. This departs substantially from a conclusion of Tanaka et al. (2012) that Arctic cyclones feature predominantly equivalent barotropic structures and random movement over the Arctic Ocean. In contrast to the genesis locations of intense Arctic cyclones in this catalog, Brummer et al. (2000) and Serreze and Barrett (2008) found that a substantial portion of summer-time Arctic cyclones developed over the Arctic Ocean. Some of the aforementioned disagreement is likely explained by the restriction of this study and Clancy et al. (2022) to the most intense Arctic cyclones. It is possible that *intense* Arctic cyclones develop in baroclinic environments found further south while *weaker* Arctic cyclones not considered in this study have equivalent barotropic vertical structures associated with migratory TPV structures isolated in the high Arctic.

	Aug	Sep	Sum
2006	3	4	7
2007	3	4	7
2008	4	6	10
2009	4	7	11
2010	4	3	7
2011	4	8	12
2012	4	3	7
2013	4	5	9
2014	3	9	12
2015	1	9	10
2016	7	10	17
2017	5	6	11
2018	6	7	13
2019	6	7	13
2020	3	4	7
Sum	61	92	153
Mean	4	6	-
Median	4	6	-
Mode	4	4	-
σ	1	2	-
Max	7	10	-
Min	1	3	-

TABLE 2.1: Counts and basic statistics for all intense Arctic cyclones during August and September, 2006-2020.

	Aug_i	Sep_i	Sum_i
2006	1	4	5
2007	2	1	3
2008	2	3	5
2009	1	5	6
2010	3	1	4
2011	2	3	5
2012	3	1	4
2013	3	2	5
2014	1	5	6
2015	0	5	5
2016	7	5	12
2017	3	1	4
2018	3	3	2
2019	1	1	2
2020	0	1	1
Sum	32	41	73
Mean	2	3	-
Median	2	3	-
Mode	3	1	-
σ	2	2	-
Max	7	5	-
Min	0	1	-

TABLE 2.2: Counts and basic statistics for all intense, ice-interacting Arctic cyclones (subscript i) during August and September, 2006-2020.

	Chu	Sib	Lap	Kar	Bar	Nor	Grn	Baf	Can	Bea
1-15 Aug	1	2	3	6	4	0	0	0	2	0
16-31 Aug	0	1	4	3	5	3	2	0	3	2
1-15 Sep	1	1	2	3	4	6	5	1	3	2
16-30 Sep	0	2	3	4	7	7	8	0	2	1

TABLE 2.3: The number of intense, ice-interacting Arctic cyclones within each Arctic sea during the specified period, 2006-2020. Note that a given cyclone may cross through multiple seas.

FIGURE 2.1: a.) All intense Arctic cyclones during August and September, 2006-2020 (N = 153).

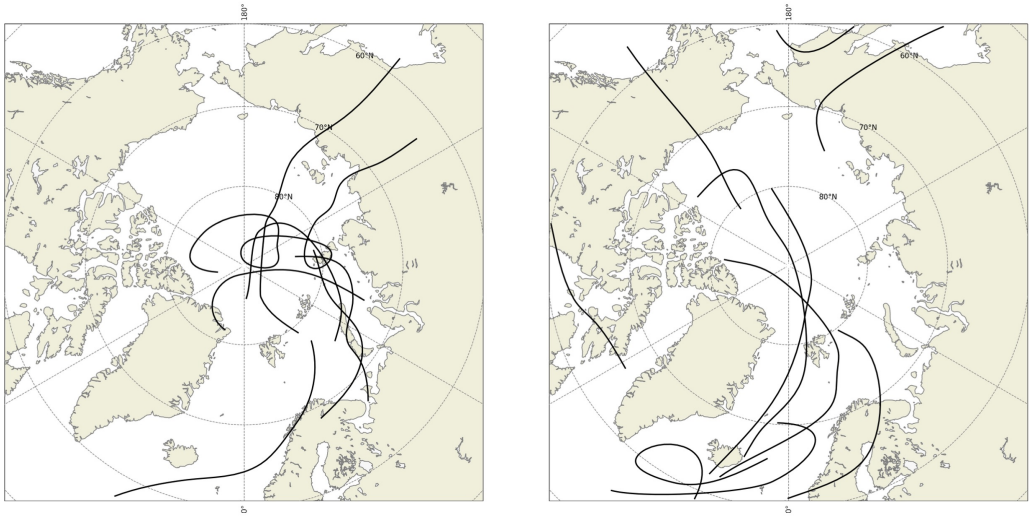

FIGURE 2.2: a.) Arctic storm tracks during August 2016, the stormiest August in the Arctic from 2006-2020 ($N = 7$). b.) as for a. but for September 2016 ($N = 10$).

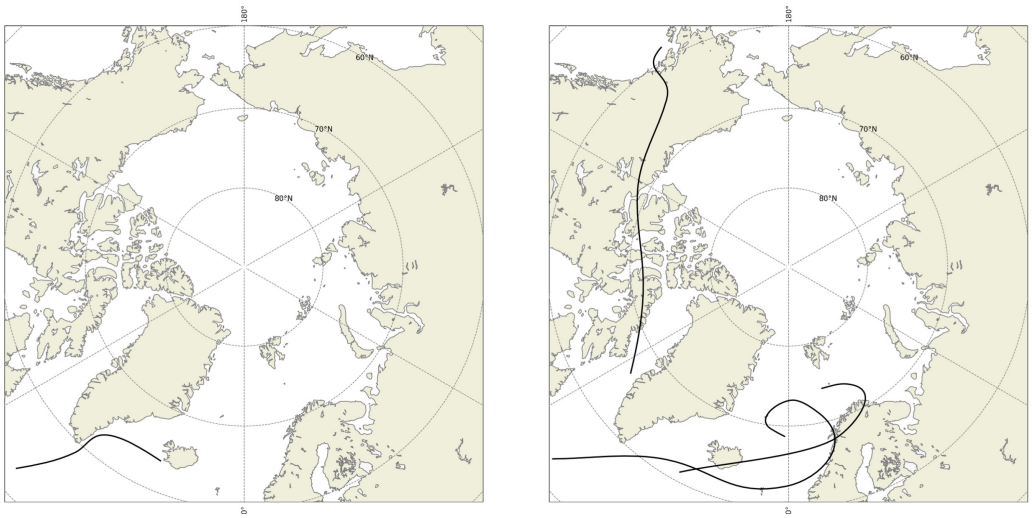

FIGURE 2.3: a.) Arctic storm tracks during August 2015, the least stormy August in the Arctic from 2006-2020 ($N = 1$). b.) as for a. but for September 2012 ($N = 3$).

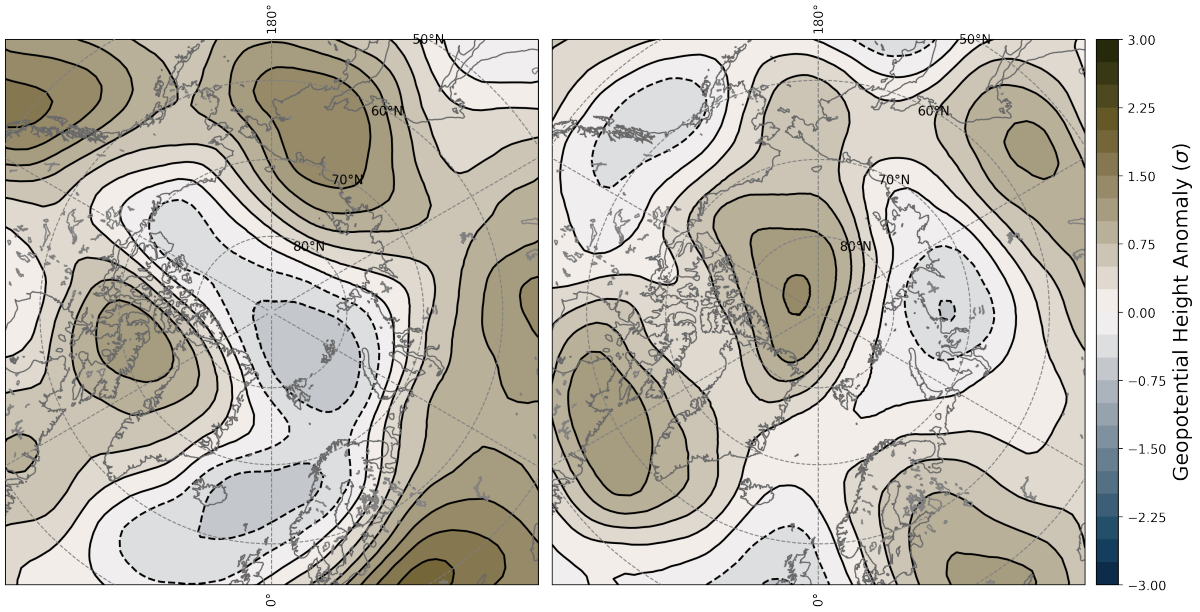

FIGURE 2.4: a.) 4-month composite of standardized 500 hPa geopotential height anomalies for stormiest Augusts. b.) As in a. but for quiescent Augusts.

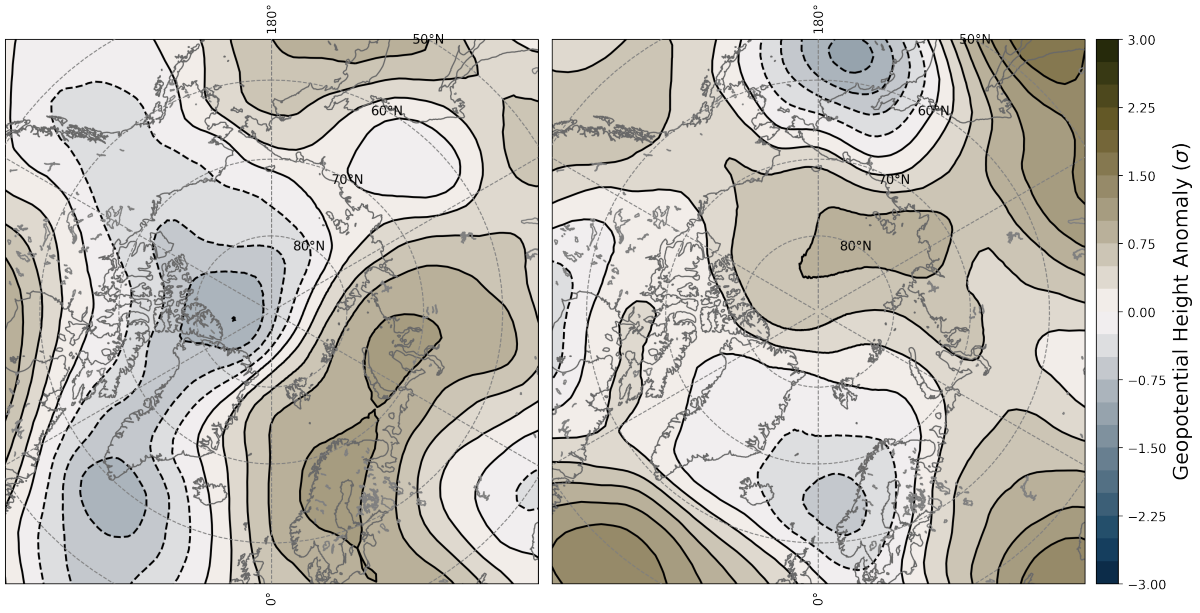

FIGURE 2.5: a.) 4-month composite of standardized 500 hPa geopotential height anomalies for stormiest Septembers. b.) As in a. but for quiescent Septembers.

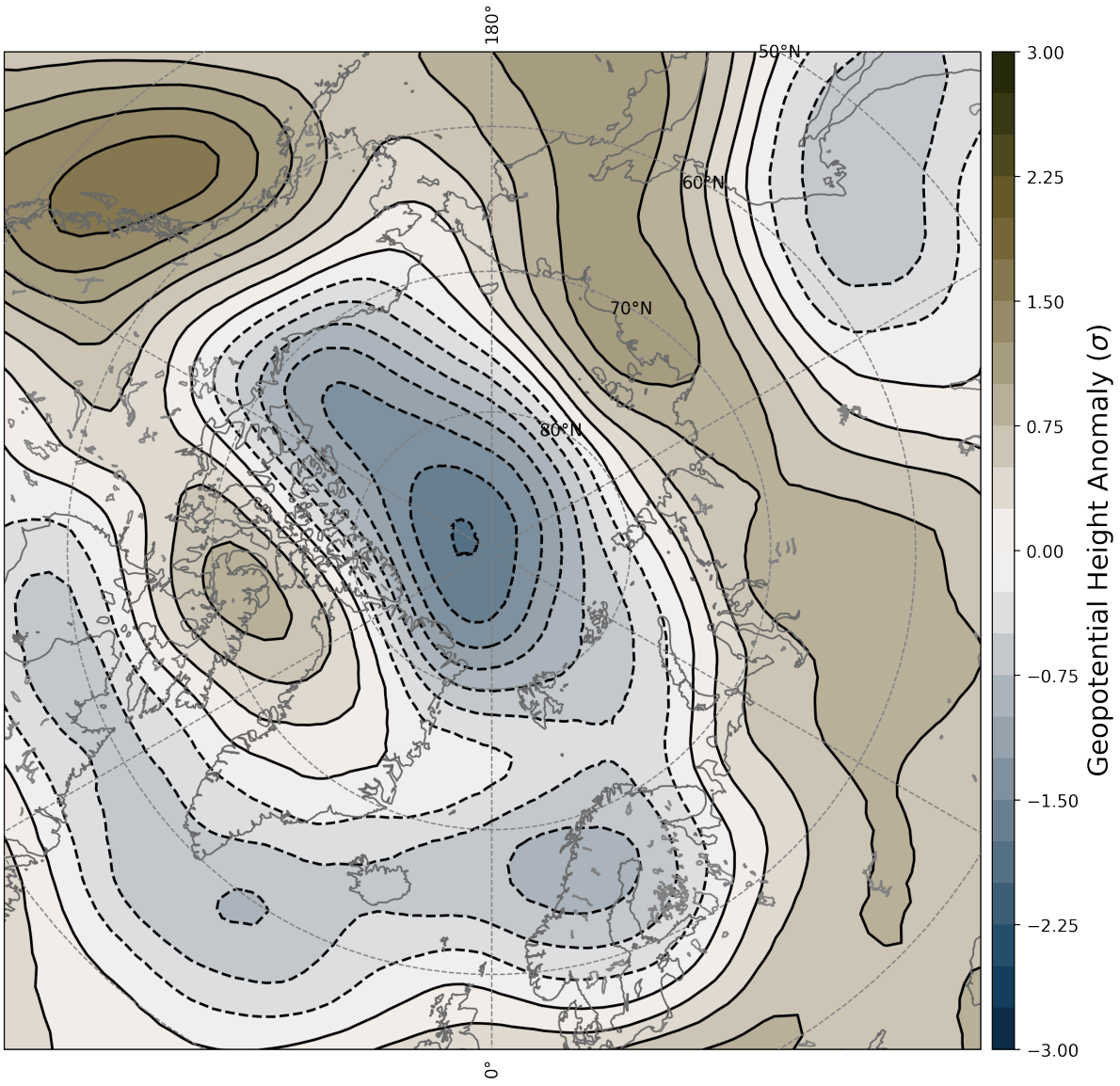

FIGURE 2.6: Difference between stormy and quiescent August standardized 500 hPa geopotential height anomalies

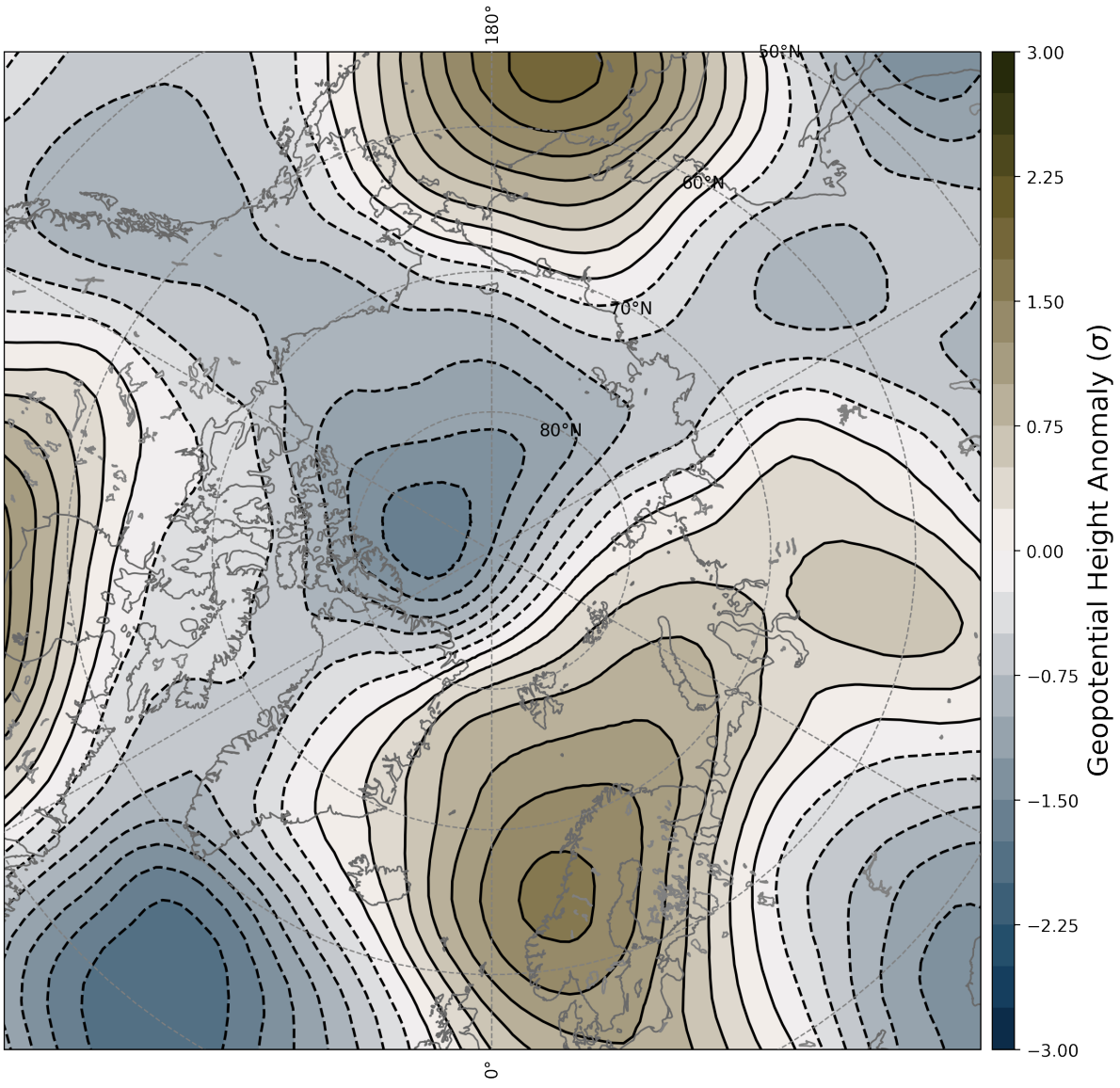

FIGURE 2.7: Difference between stormy and quiescent September standardized 500 hPa geopotential height anomalies.

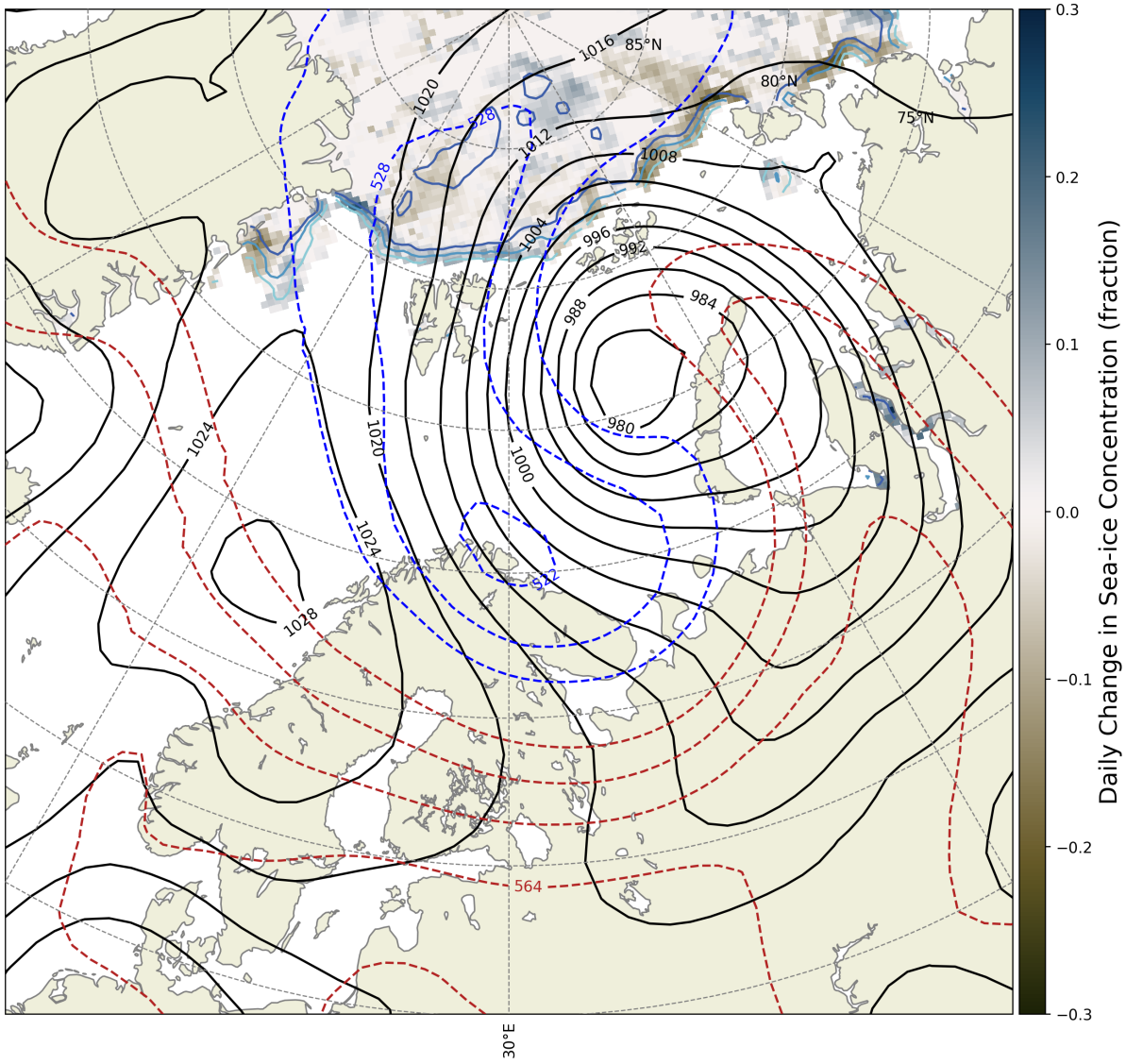

FIGURE 2.8: Sea-level pressure (solid black every 4 hPa), 1000-500 hPa thickness (blue every 60 dam changing to red at 540 dam) and daily sea-ice concentration change (colormesh) at 00Z 16 August 2016.

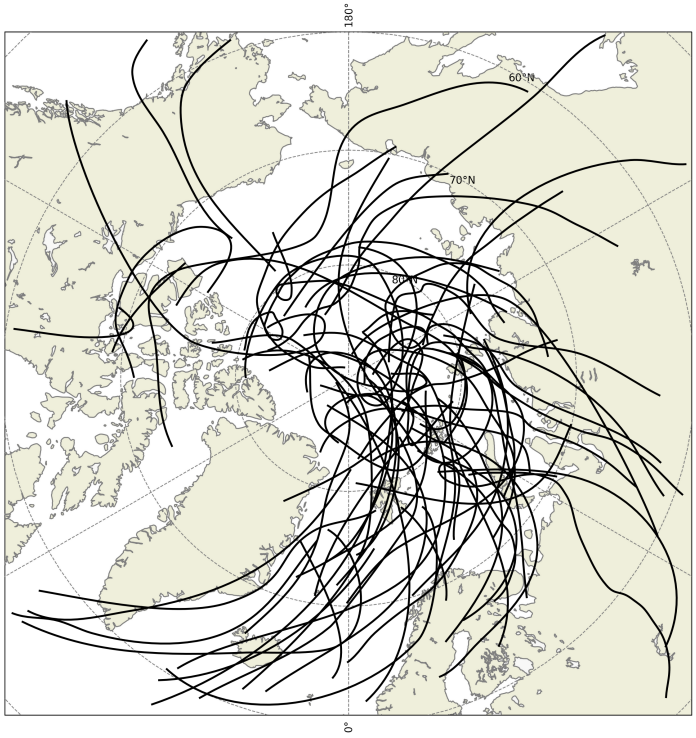

FIGURE 2.9: a.) All intense cyclones during August and September which interacted with Arctic sea-ice, 2006-2020 ($N_i = 73$).

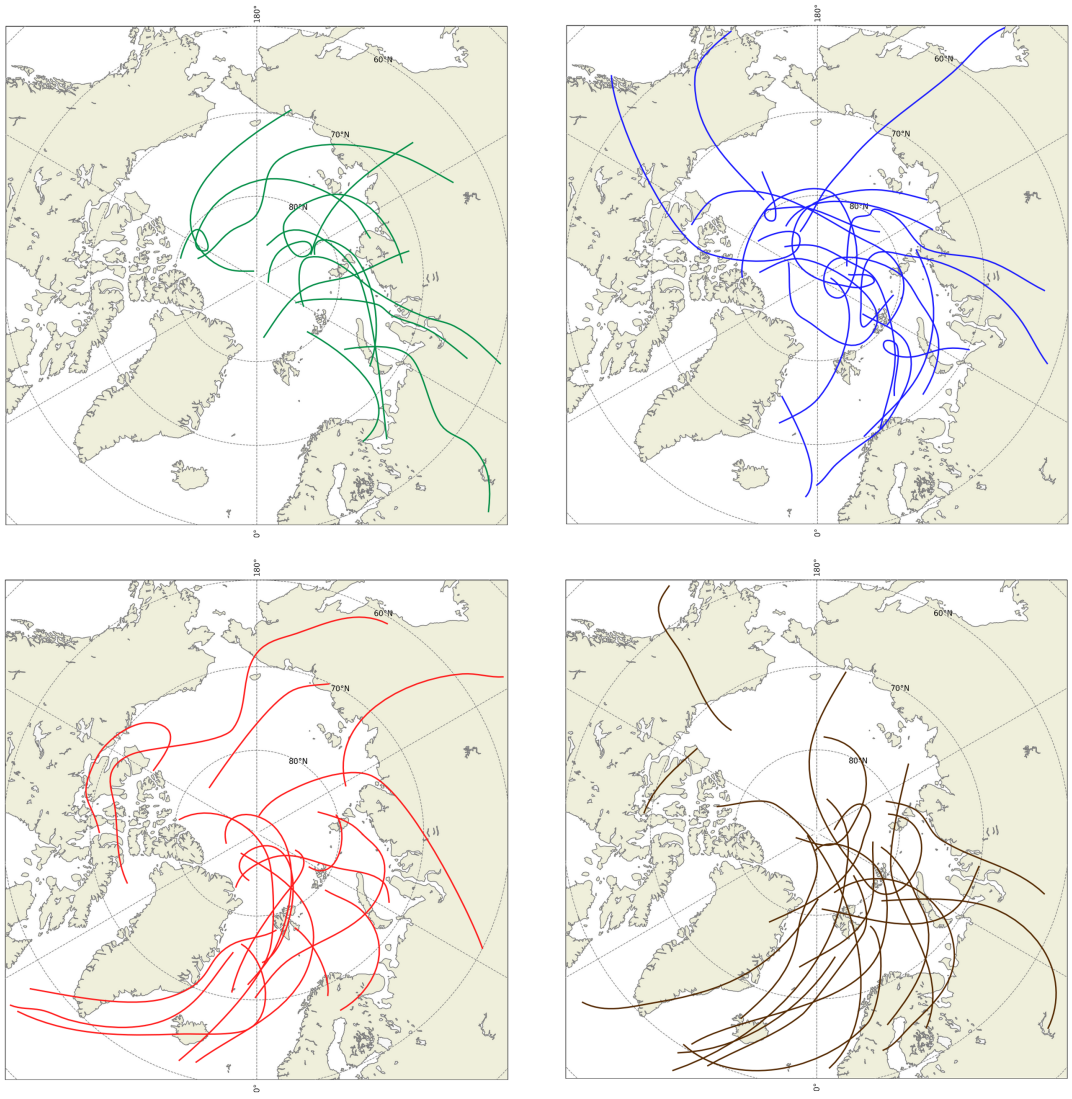

FIGURE 2.10: a.) As in Fig. 2.1 but for 1-15 August ($N_i = 12$). b.) for 16-31 August ($N_i = 16$). c.) for 1-15 September ($N_i = 18$). d.) 16-30 September ($N_i = 18$).

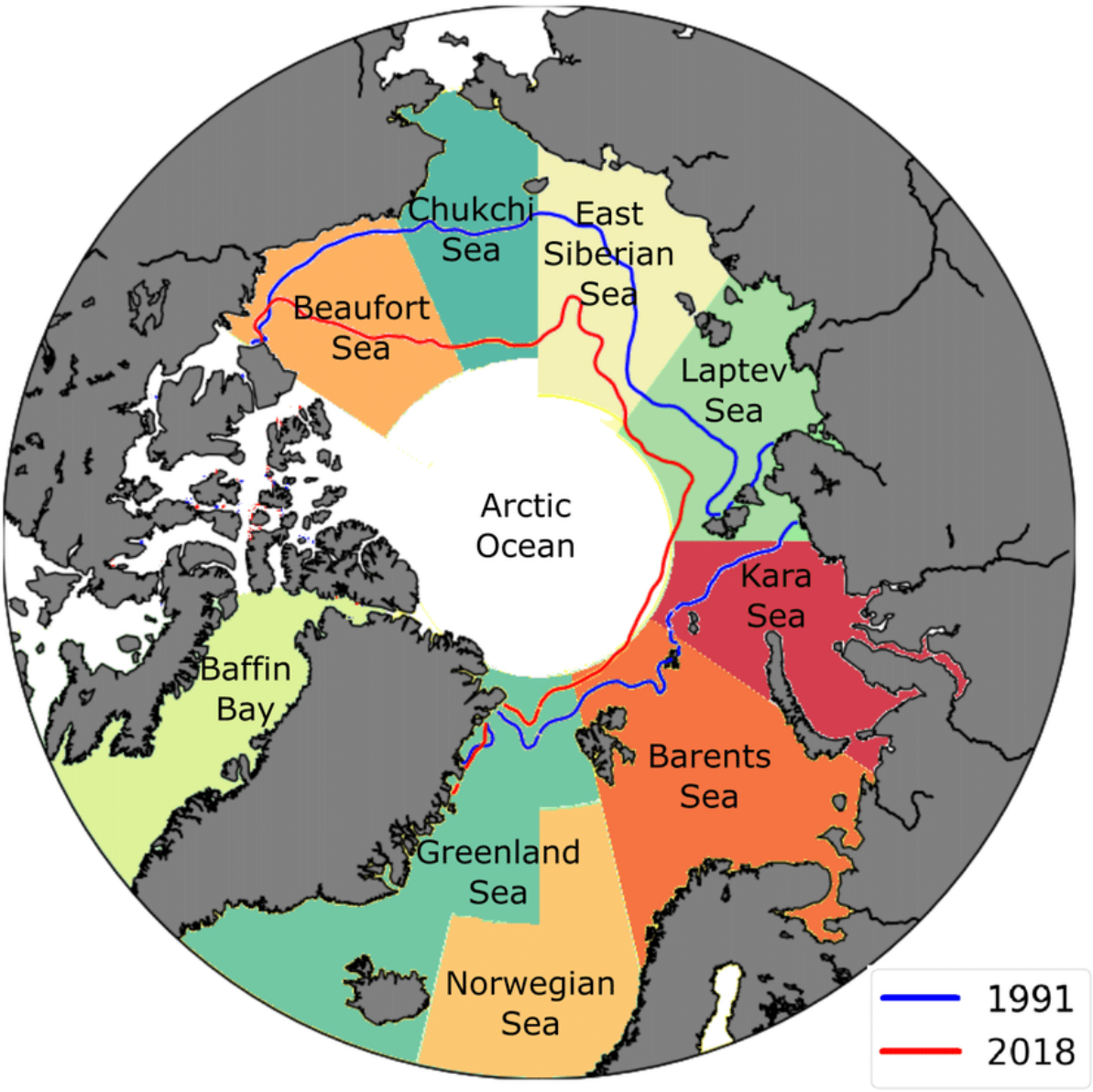

FIGURE 2.11: Arctic sea boundaries defined by the International Hydrographic Organization, available online at http://www.marineregions.org/. Map from Cabral et al. (2022) includes European Reanalysis minimum sea-ice extent for 1991 and 2018.

Chapter 3

Development of an intense cyclone and its interaction with sea ice

3.1 The cyclone life-cycle

3.1.1 Motivation

In order to better understand the structural characteristics of individual catalog members, the life-cycle of an intense August cyclone which interacted with Arctic sea ice is interrogated using JRA55 reanalysis data and CloudSat/CALIPSO precipitation and cloud-radiative products. One event which occurred in mid-August 2010 benefited from overpasses (granules) providing insights into the cloud and precipitation distribution within the cyclone's robust occluded thermal ridge structure. These granules coincided with a

period of robust sea-ice concentration changes in the eastern Arctic Sea thought to be associated with the cyclone's circulation and cloud-radiative effects (CRE).

3.1.2 Methods

The primary characteristics of the cyclone's life-cycle are investigated using daily analysis of sea-level pressure, 1000-500 hPa thickness, 500 hPa geostrophic relative vorticity (only analyzed south of 80N) and precipitable water (PWAT). Since the thermal wind blows along thickness contours with low thickness to the left (in the Northern Hemisphere), the aforementioned charts allow qualitative evaluation of the Sutcliffe-Trenberth form of the quasi-geostrophic omega equation (Sutcliffe, 1947, Trenberth, 1978)

$$\sigma\left(\nabla^2+\frac{f_0^2}{\sigma}\frac{\partial^2}{\partial p^2}\right)\omega=2\left[f_0\frac{\partial\vec{V}_g}{\partial p}\cdot\nabla(\zeta_g+f)\right], \tag{3.1}$$

where ω is the synoptic-scale vertical motion. While (3.1) neglects deformation and diabatic processes, it diagnoses the primary component of forcing for synoptic-scale vertical motion, absolute geostrophic vorticity advection by the thermal wind. Sutcliffe (1947) relates the quantity on the RHS directly to the net mass divergence within a column. Since the surface pressure depends on the mass of the overlying column, (3.1) is equivalently a diagnostic regarding the development of surface pressure systems. For our purposes,

upward (downward) vertical motion and a decrease (increase) in the surface pressure is consistent with cyclonic vorticity advection (CVA) by the thermal wind.

The classical analysis maps described above are complimented by daily visible satellite mosaics (available online at https://worldview.earthdata.nasa.gov) and CloudSat/CALIPSO granules (available online at https://www.cloudsat.cira.colostate.edu). CloudSat features a 94-GHz Cloud Profiling Radar while CALIPSO features a Cloud-Aerosol Lidar with Orthogonal Parameterization. This A-train satellite pair provides high-resolution data regarding cloud phase (2B-CLDCLASS-LIDAR), cloud radiative effects (2B-FLXHR-LIDAR), precipitation type (2C-RAIN & SNOW-PROFILE) and radar reflectivity (2B-GEOPROF). Column integrated short-wave and long-wave radiative effect products were summed to produce a net bottom-of-atmosphere CRE variable. Radar reflectivity data was converted from height to pressure coordinates using the US standard atmosphere.

3.1.3 Results

3.1.3.1 Synoptic-dynamic environment

At 00Z on 14 August 2010 a summer cyclone developed immediately east of Greenland in a region of moderate baroclinicity extending from the Greenland Plateu towards the Barents Sea (Fig. 3.1a). This cyclone was situated immediately downshear of an upper-level geostrophic vorticity anomaly, a region characterized by CVA by the thermal wind and upward vertical motion via equation (3.1). A visible satellite mosaic taken around

this time indicates pervasive cloudiness in portions of the Greenland and Norwegian Seas and Scandinavia, generally down-shear of the cyclone center (Fig. 3.1b).

Distinct frontal regions emerged over the following 24 hours as the cyclone deepened by approximately 12 hPa while moving to just north of Sweden (Fig. 3.2a). Moisture had organized into an axis of strongly anomalous PWAT immediately in advance of the cyclone's sweeping cold front which presented as a distinct comma-tail cloud feature (Fig. 3.2b). Still located in a region of CVA by the thermal wind, the cyclone continued development over the subsequent 24 hours before attaining a closed 980 hPa isobar to the northwest of Novaya Zemlya by 00Z 16 August (Fig. 3.3a). At this time the cyclone met the criteria for classification as an intense, ice-interacting Arctic cyclone as described in Section 2.3.

Upon reaching maturation, this robust surface cyclone had become well occluded with an axis of high thickness and PWAT anomalies stretching from coastal Eurasia towards Zemlya Georga (Fig. 3.4a). This occluded thermal ridge structure was characterized by heavy cloud cover (Fig. 3.4b) linking the peak of the residual warm-sector to the cyclone center. The cyclone became vertically stacked with the upper-level geostrophic vorticity feature by 00Z 17 August such that the thermal wind was largely pointed along vorticity contours (Fig. 3.4a). The primary cloud and precipitation feature in this post-mature cyclone was thus the pervasive occluded thermal ridge structure (Fig. 3.4b). A single CloudSat/CALIPSO transect intersected this cloud feature in two places: once over open ocean southwest of the cyclone center, and again to the northeast, immediately adjacent

to a portion of the ice-edge characterized by pronounced losses in sea-ice concentration (Fig. 3.4c).

3.1.3.2 Satellite observations

A cross-section taken along the CloudSat granule from A-A' (see Fig. 3.4) around 00Z 17 August reveals the structural characteristics of the occluded thermal ridge structure: an axis of poorly stratified, high equivalent potential temperature air extending throughout much of the free-troposphere (as indicated by the grey and black stars in Fig. 3.5). The heart of the occluded thermal structure is characterized by low potential vorticity air reminiscent of a sub-tropical environment (black star). The rarity of such an airmass at 80N is indicated by 3σ precipitable water vapor anomalies co-located with the axis of low potential vorticity air (Fig. 3.4a & Fig. 3.5). Some radar returns in this region extended well into the upper-troposphere, apparently interacting with the upper-troposphere, lower-stratosphere as indicated by the jagged nature of the overlying dynamic tropopause. This is in contrast to relatively shallow radar returns to the southwest (grey star).

Several other differences arise when considering the two portions of the occluded thermal ridge structure. Firstly, note that the portion closer to A (grey star) is characterized by cooler temperatures in the lower troposphere (Fig. 3.5). The presence of some liquid clouds in this region indicates a near-freezing surface environment (Fig. 3.6a) and snowfall was observed in excess of 10 mm hr^{-1} (Fig. 3.6c) immediately along the axis of weak stratification (Fig. 3.5, grey star). The heart of the thermal ridge structure (black star) is

characterized by warmer temperatures in the lower troposphere (Fig. 3.5). A light rainfall rate of approximately .008 mm hr^{-1} was observed immediately in the warm core of that structure (Fig. 3.6c).

The long-wave effect is remarkably consistent between these two regions of cloudiness in spite of the aforementioned differences in thermodynamic and precipitation characteristics (Fig. 3.6b). That said, the *net* CRE of these clouds differs dramatically due to the reflection of incoming short-wave radiation by high clouds in the heart of the thermal ridge (black star). Here the short-wave effect overwhelms downward emitted long-wave radiation such that the net CRE is to cool the surface. The relatively weak short-wave effect associated with lower clouds to the southwest (grey star) results in a net positive CRE such that clouds act to warm the surface. Given that these two cloud-heads are part of one, continuous phenomena, it follows that the net CRE changes sign somewhere along the thermal ridge structure.

3.2 Arctic sea ice

3.2.1 Methods

As additional motivation, this case-study compliments the analysis of Mundi (2022) which described changes in the sea-ice distribution along the marginal ice zone during this particular event. In their analysis, changes in the sea-ice area were analyzed in a domain defined by the maximum and minimum longitudinal and latitudinal extents of the 1000 hPa contour from 15-17 August (approximately 30-90E, 70-85N, see Fig. 3.7). Although

this novel methodology was repeatable for several different cyclones, it is potentially problematic in this application.

Synoptic analysis of this mid-August cyclone indicates that the area enclosed by the 1000 hPa contour fails to capture the entire circulation of the cyclone. For example, even the 1020 hPa contour exhibits cyclonic curvature west of Svalbard and well poleward of 87N on the 17th (Fig. 3.4a). This indicates that the analysis of Mundi (2022) may have inadvertently included sea-ice transport through the northern boundary of the domain (the 85th parallel). In addition, the extent of the 1000 hPa contour over coastal Eurasia on 16 and 17 August indicates that the vast majority of their chosen domain was not covered in sea ice, potentially diluting the magnitude of observed changes in sea-ice area. It was established in Section 2 that the common signature of a robust cyclone/sea-ice interaction is a dipole in sea-ice concentration changes straddling the cyclone center. Since one goal of this case-study is to determine whether the cyclone imposed a net change in ice area (rather than just a rearrangement), an alternate domain chosen for this analysis was thought to better represent the impact of the greater cyclone circulation.

In order to investigate the effect of the mid-August 2010 cyclone on local sea-ice, the area of Arctic sea-ice was calculated in a domain spanning 345-90E, 75-88.75N using JRA55 data at 6-hr temporal and 1.25° spatial resolution (Fig. 3.7). Maps of daily sea-ice concentration change throughout the storm period (see Section 2.3, Fig. 3.1c-Fig. 3.4c & Fig. 3.8) indicate the chosen domain contains the vast majority of the sea-ice shelf subjected to rearrangement processes while simultaneously limiting the inclusion of open

ocean. Given the persistence of off-ice flow partially associated with the remnant cyclone from 18-21 August (Fig. 3.8), the storm period was regarded as 14-21 August.

3.2.2 Results

3.2.2.1 Local changes in sea-ice concentration

At 00Z 14 August the predominant synoptic feature in the Barents Sea was a weak 1008 hPa cyclone (Fig. 3.1c). Over the following 24 hours the cyclonic circulation associated with this weakening cyclone appeared to impose a dipole in daily sea-ice concentration change where there was a component of flow across the ice edge (Fig. 3.2c). By this time, however, an intensifying cyclone immediately northeast of Sweden had begun to envelope the broader Barents and Greenland Seas. This cyclone developed dramatically into 00Z 16 August (see Section 3.1), its circulation now stretching from approximately 0-90E. Daily losses in sea-ice concentration were most notable at 00Z 17 August when the occluded thermal ridge structure occupied the ice-shelf in a region of strong on-ice flow (Fig. 3.4c).

From 14-17 August the portion of the ice edge extending from eastern Greenland to the waters immediately east of Svalbard are characterized by a relatively strong sea-ice concentration gradient (Fig. 3.1c-Fig. 3.4c). This region was subject to increasingly strong off-ice flow between 15-17 August. Given that the local sea-ice concentration tendency represents the sum of advection and other ice processes, it is unclear from this analysis alone which of these processes dominates. Given the low thickness values between

Greenland and Svalbard from 15-17 August, it is presumed that along-transport freezing processes are important.

This is in stark contrast to the portion of ice immediately east of Svalbard characterized by on-ice flow and daily sea-ice concentration losses (Fig. 3.1c-Fig. 3.4c). Here the sea-ice concentration gradient appears relatively diffuse, increasingly so under continued influence of on-ice flow from 15-17 August (Fig. 3.2c-Fig. 3.4c). At 00Z 17 August, a region of pronounced sea-ice concentration loss extending hundreds of kilometers onto the ice shelf was co-located with a portion of the occluded, thermal ridge structure (Fig. 3.4c). While on-ice flow occurred in a relatively broad swath extending from Zemlya Georga, the 0.8 sea-ice concentration contour retreated in a very narrow region characterized by the occluded cloud-head. The portion of this cloud-head sampled nearest the region of sea-ice losses was associated with a net negative CRE indicating that those clouds were contributing to local cooling (Fig. 3.6b). Since net radiative cooling was coincident with a region of pronounced decreases in sea-ice extent, it is concluded that the local ice distribution is primarily a function of the cyclone circulation.

3.2.2.2 Sea-ice area

The observed sea-ice area within a domain spanning 345-60E, 75-88.75N is plotted at 6-hr intervals during August 2010 and compared with the simple linear trend over that period (Fig. 3.9a). At 00Z 14 August, immediately prior to cyclogenesis, there were approximately 7.1×10^{11} m^2 of sea-ice within the domain, only slightly more than that

expected from the linear trend. The sea-ice area remained relatively stagnant as the cyclone strengthened over the subsequent 24 hours. On the 16th, however, the domain began to rapidly lose sea-ice area before reaching a local minima of approximately 5.5×10^{11} m^{-2} on 18 August. By this time the surface cyclone was located at the southern tip of Novaya Zemlya and winds throughout the domain were backing towards the off-ice direction (Fig. 3.8a). Off-ice flow continued between 00Z 19 and 00Z 21 August as the occluded cyclone continued to weaken east of Novaya Zemlya, a period characterized predominantly by local sea-ice concentration gains (Fig. 3.8b-c). The total sea-ice area increased dramatically during this time (Fig. 3.9a).

The 3-day running mean of 6-hr changes in sea-ice area was calculated for August 2010 and set in comparison to the August 2006-2020 climatological 6-hr sea-ice concentration change. This climatological value was calculated by dividing the difference between the 15-year domain-average sea-ice area at 18Z 31 August and 00Z 1 August by the number of 6-hr periods in that temporal range. This indicates that, on average, the domain loses approximately 2.5×10^9 m^2 of sea ice every 6-hrs during the month of August. During the storm period more ice was lost than that expected by climatology (Fig. 3.9b). Losses were most pronounced between 17 and 19 August, the period over which the cyclone underwent cyclolysis in the Kara Sea (Fig. 3.4c & Fig. 3.8a-b). Once the domain was characterized primarily by off-ice flow, however, the sea-ice area began to increase, so much so that the 3-day running mean sea-ice area change was above climatology on 20 and 21 August. At the end of the storm period (00Z 21 August) the 3-day running mean sea-ice area change was actually positive. That said, the sum of all 6-hr changes in sea-ice

area during the storm period indicates that a net loss of sea-ice, compared to climatology, occurred in association with the development and passage of this cyclone over the region.

3.3 Discussion

The intense Arctic cyclone of mid-August 2010 clearly developed via the release of baroclinic instability. In this case an upper-level geostrophic vorticity anomaly was located immediately upstream of a surface cyclone in a moderately sheared environment. Low-level temperature advection associated with the low-level circulation of this incipient development led to the rapid amplification of the upper-level thickness and vorticity fields. In turn, CVA by the thermal wind intensified near the cyclone center, further lowering the surface pressure, and, thus, intensifying the low-level temperature advections. This positive feedback is consistent with a poleward heat flux and results in the reversal of the thickness gradient relative to climatology on 16 and 17 August (i.e. Rossby wave breaking, Fig. 3.4a). The warm, anomalously moist region isolated in the eastern Arctic had low potential vorticity and 3σ PWAT anomalies indicative of Mediterranean (subtropical) origin. At the end of its baroclinic life-cycle the surface cyclone became vertically stacked with the upper-level geostrophic vorticity feature associated with its development. This equivalent barotropic feature was no longer able to encourage further development.

The aforementioned, baroclinic life-cycle is in agreement with a conclusion of Clancy et al. (2022) that most Arctic cyclones develop in sheared environments. This is in contrast

to the prevailing notion that Arctic cyclones are typically equivalent barotropic or axisymmetric (e.g. Aizawa and Tanaka, 2016, Tanaka et al., 2012). In this case, the rapid development and subsequent occlusion of a robust, baroclinic cyclone results in an equivalent barotropic structure. Such disparate views regarding the nature of Arctic cyclones as either baroclinic (e.g. Clancy et al., 2022) or equivalent barotropic (e.g. Aizawa and Tanaka, 2016, Tanaka et al., 2012) are seemingly misleading and at odds with descriptions of the characteristic life-cycles of observed events. The analysis method chosen for this mid-August event indicates that one can describe the first-order evolution of an intense Arctic cyclone between baroclinic and equivalent barotropic states with remarkably few atmospheric variables and a straightforward diagnostic equation. Such methodology is generally lacking in other case-studies of Arctic cyclones (e.g. Blechschmidt et al., 2016, Simmonds and Rudeva, 2012, Tanaka et al., 2012, Yamagami et al., 2017).

Given the relative dearth of radar observations in high latitudes, CloudSat/CALIPSO bolster the aforementioned synoptic-dynamic analysis by providing insights into the precipitation distribution and radiative effects of clouds associated with Arctic cyclones. In this case, a transect nearly exactly across the cyclone's occluded, thermal ridge structure confirms that the primary generation region of clouds and precipitation within the occluded cyclone was an axis of poorly stratified, high θ_e air in the middle troposphere. Short-wave radiation reflected by these clouds may partially or completely offset long-wave radiation emitted towards the surface. This indicates that the net effect of clouds on the surface depends on the characteristics of the clouds themselves, the season, and the time of day. It is hypothesized that the interaction between clouds and sea-ice is most

complex in the summer-time when the Arctic is most exposed to incoming solar radiation. In this case, observations of sea-ice concentration changes indicate that the role of clouds in rearranging ice was secondary to the influence of the cyclone's circulation.

Analysis of the domain-wide sea-ice area indicates that the presence of the Arctic cyclone was associated with a net loss in sea-ice area relative to climatology. While this analysis method can be applied to different Arctic cyclones, careful consideration of domain size and storm period must be made for each individual case. For example, long-lived cyclones with complex paths (like some of those observed at very high latitudes) may require substantially larger domains, potentially including the effect of other cyclones or phenomena on its periphery. In spite of this caveat, such analyses are necessary to clearly attribute changes in sea-ice area to the development and passage of Arctic cyclones. Even if the direction of changes are not immediately clear, it is evident that Arctic cyclones which interact with sea ice are associated with robust ice rearrangement and pronounced changes in sea-ice area relative to climatology.

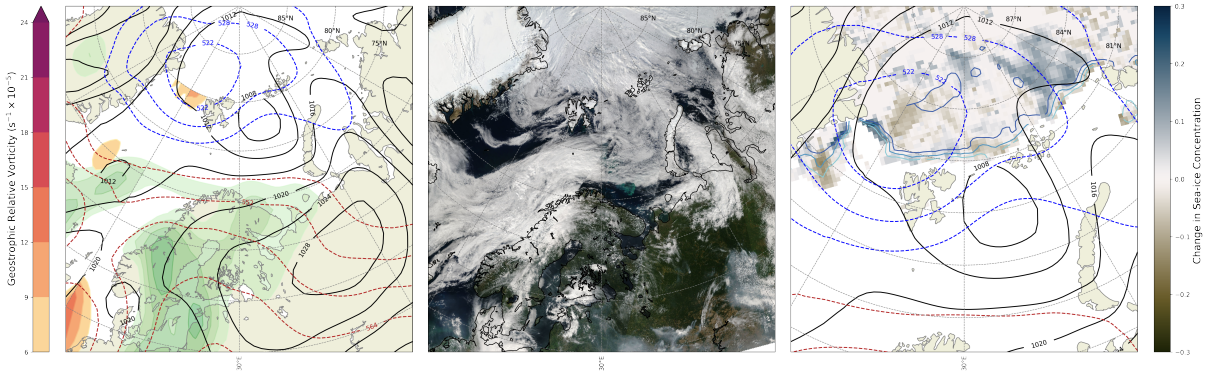

FIGURE 3.1: a.) Sea-level pressure (black contours every 4 hPa), 1000-500 hPa thickness (blue, dashed contours every 60 dam changing to red at 540 dam), standardized total column water vapor anomaly (filled greens every .5 σ starting at 1 σ and geostrophic relative vorticity (filled oranges every 3×10^{-5} s^{-1} starting at 9×10^{-5} s^{-1} at 00Z on 14 August 2010. b.) MODIS satellite mosaic around 00Z 14 August 2010 c.) Sea-level pressure (black contours every 4 hPa), 1000-500 hPa thickness (blue, dashed contours every 60 dam changing to red at 540 dam), fraction of sea-ice concentration (blue contours every .2) and daily change in sea ice concentration (blue/brown colormesh) at 00Z on 14 August 2010.

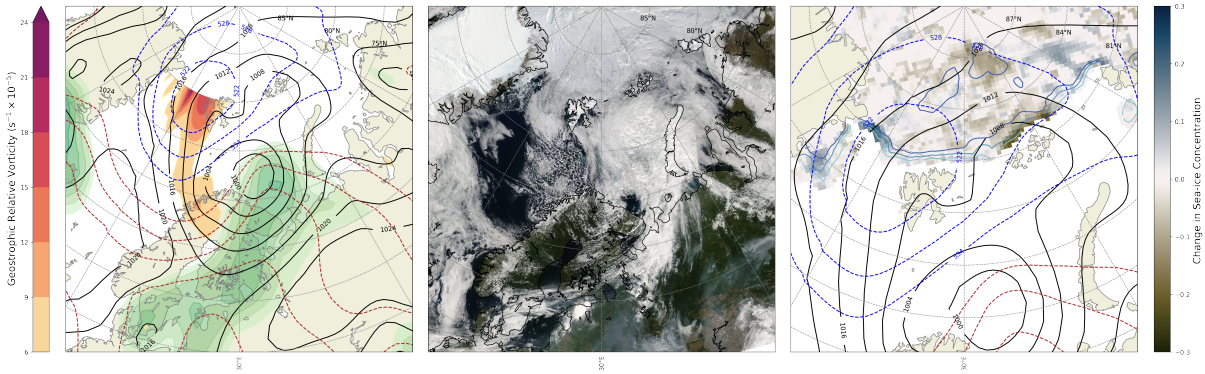

FIGURE 3.2: As in Fig. 3.1 but for 00Z 15 August.

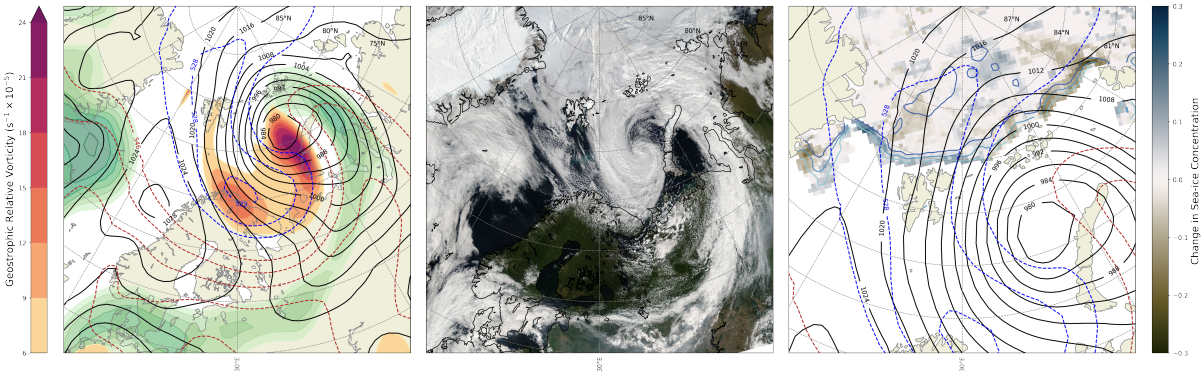

FIGURE 3.3: As in Fig. 3.1 but for 00Z 16 August.

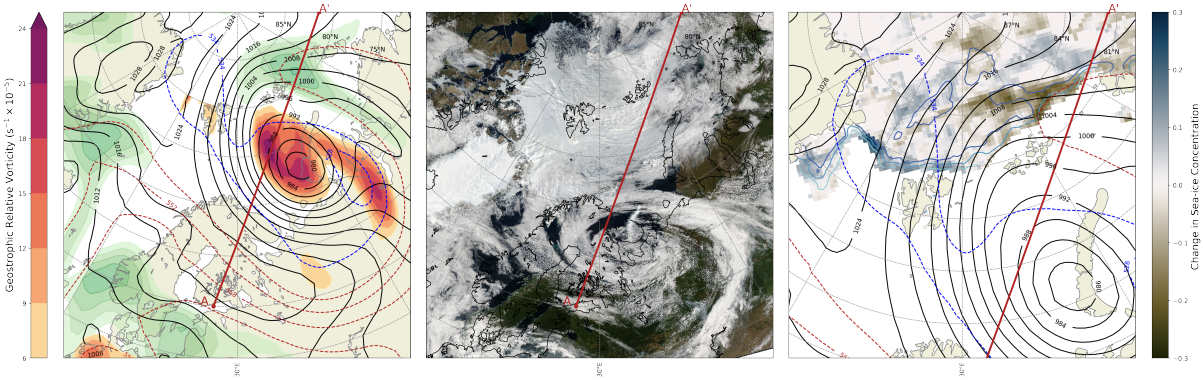

FIGURE 3.4: As in Fig. 3.1 but for 00Z 17 August.

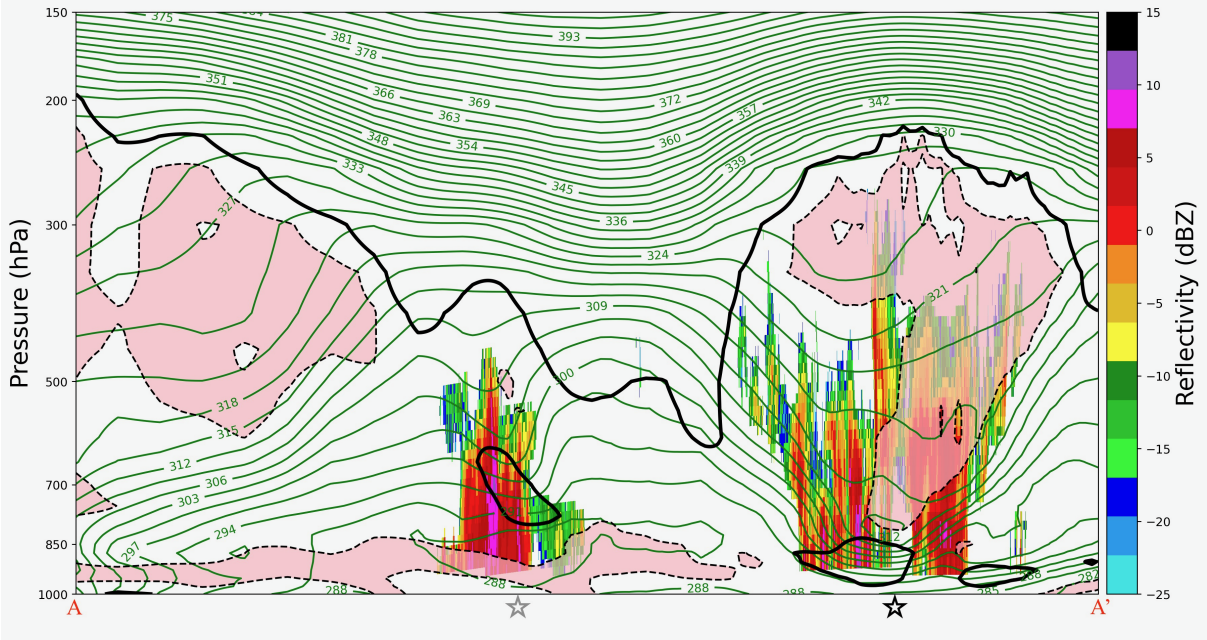

FIGURE 3.5: Equivalent potential temperature (green contours every 3 K), the dynamic tropopause (solid black at 2 PVUs), potential vorticity (dashed black contours and shaded pink from 0-.5 PVUs), and radar reflectivity (dBZ) from CloudSat granule 22887 around 00Z on 17 August 2010. The grey (black) star represents the southwestern (northeastern) portion of the intersected occluded cloud-head.

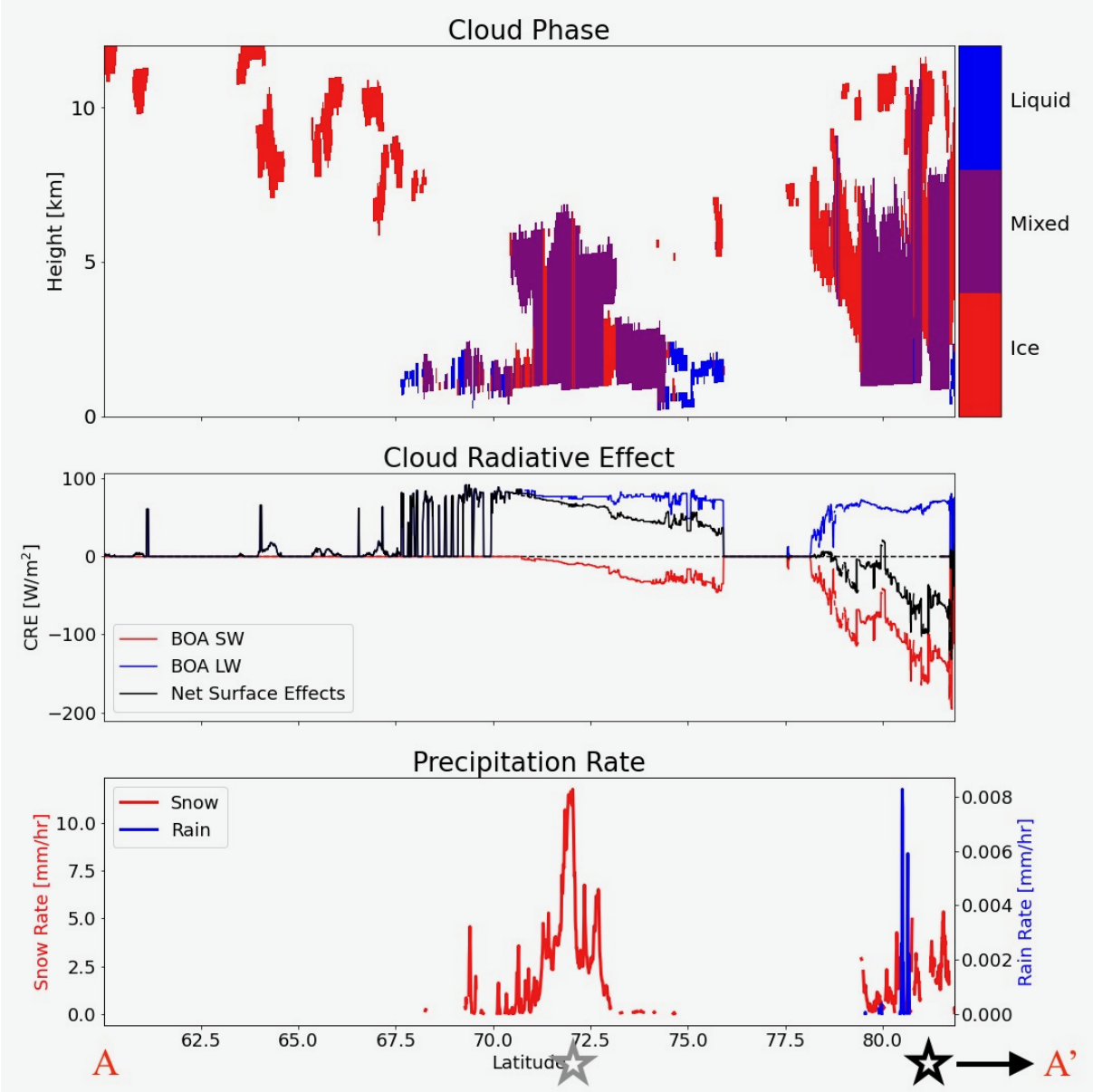

FIGURE 3.6: a.) Cloud phase from CALPISO granule 22887 around 00Z on 17 August 2010. b.) as for a.) but for cloud radiative effect. c.) as for a.) but for precipitation rate from CloudSat granule 22887. A and A' refer to the end points of the cross-section described in Fig. 3.5. The grey (black) star represents the southwestern (northeastern) portion of the intersected occluded cloud-head.

FIGURE 3.7: The chosen domain for analysis of sea-ice area and its change during the mid-August cyclone event (heavy black). The domain employed in the analysis of Mundi (2012) is also included (dashed red).

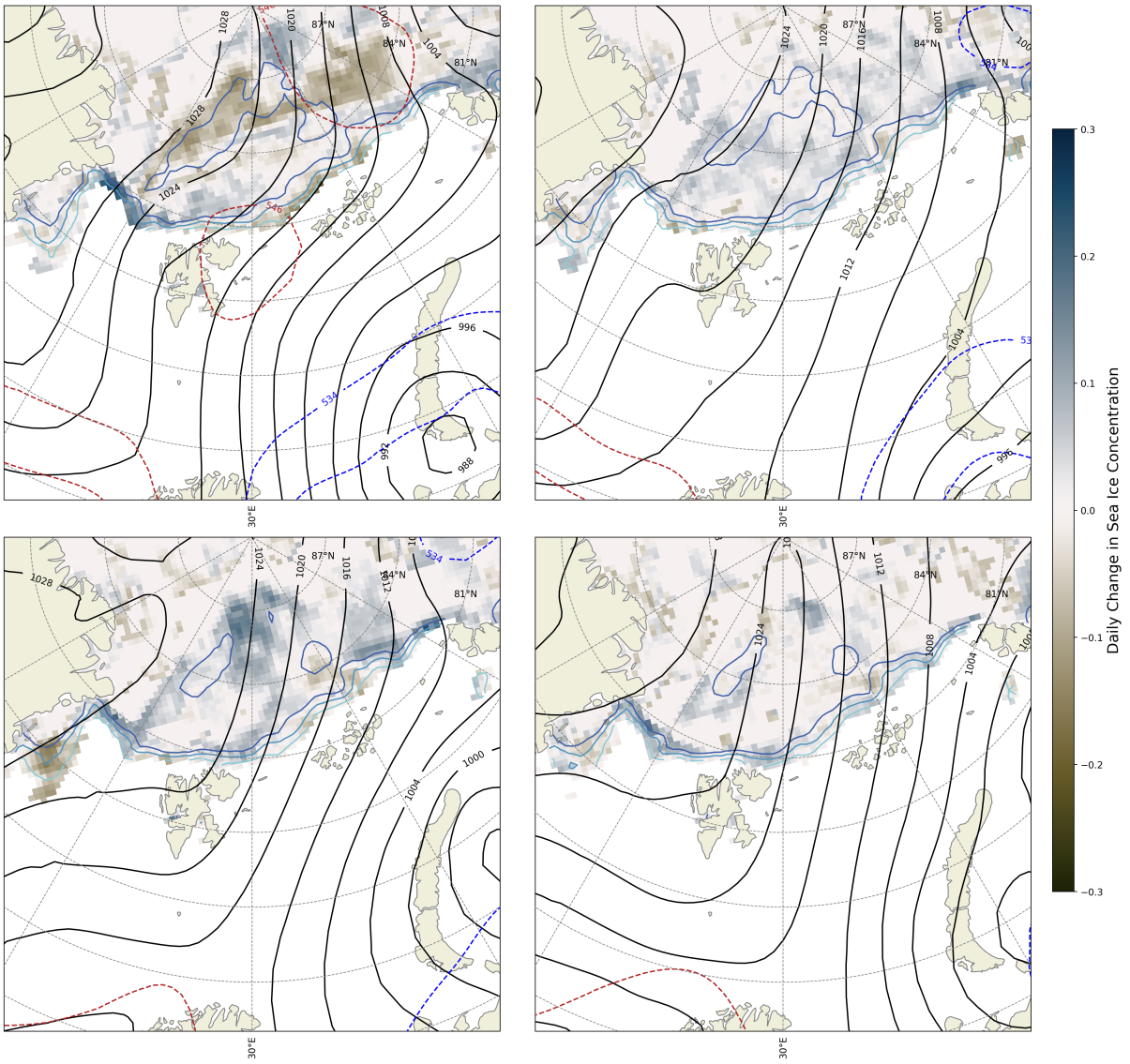

FIGURE 3.8: a.) as in Fig. 3.1c but for 18 August 2010. b.) as in a.) but for 19 August . c.) as in a.) but for 20 August. d.) as in a.) but for 21 August.

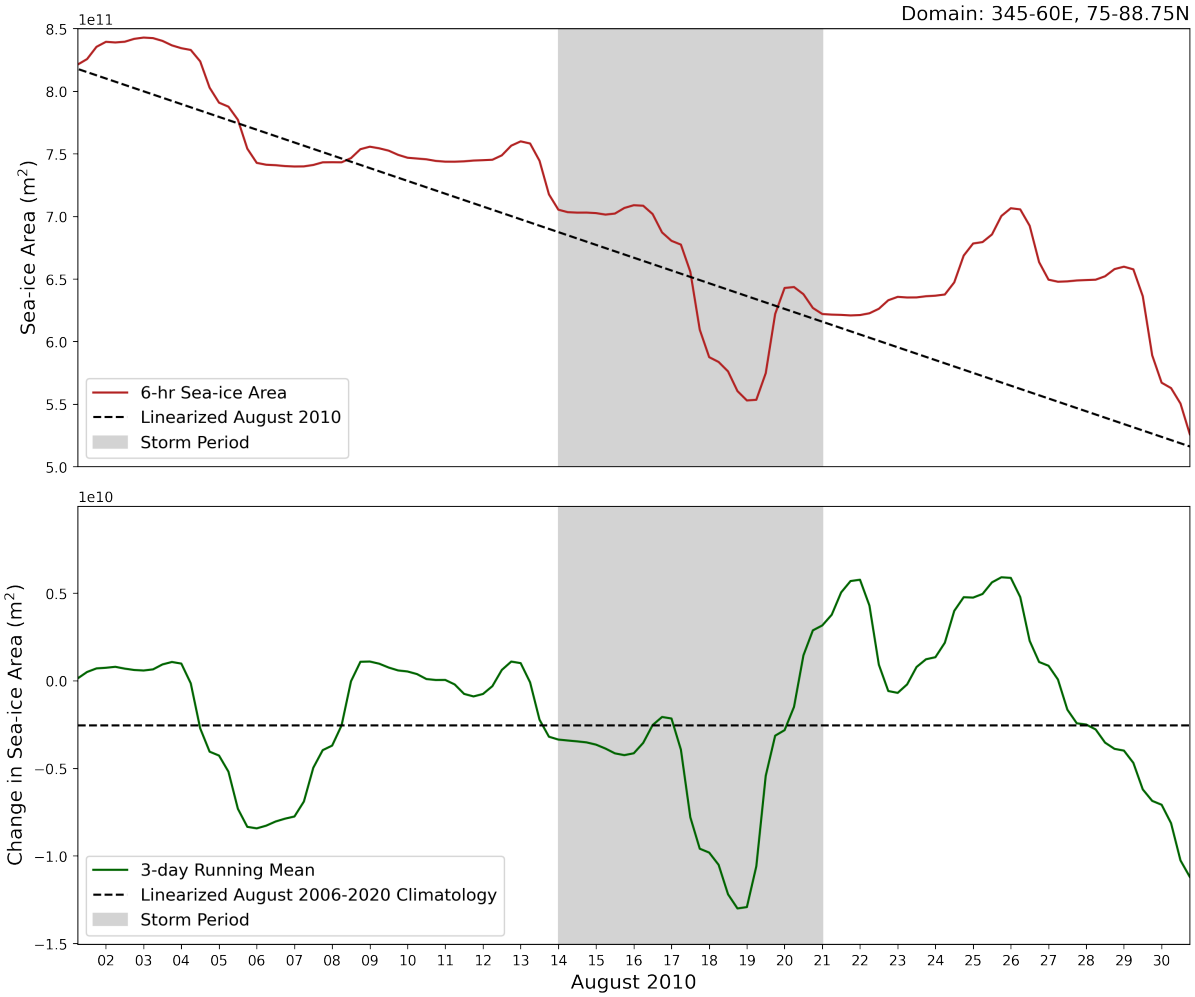

FIGURE 3.9: a.) 6-hr Sea-ice area (solid red) and its linear fit (dashed black) in the vicinity of the mid-August 2010 cyclone. The storm period is denoted in grey. b.) as in a.) but for the change in sea-ice area (solid green) and the August 2006-2015 climatological 6-hr sea-ice change (dashed black).

Chapter 4

Summary, conclusions and recommendations for future work

4.1 Climatology of intense, Arctic cyclones in late summer

A climatology of intense, Arctic cyclones which occured in the late-summer months of August and September was formed to cover the first 15 years of the CloudSat/CALIPSO satellite-era, 2006-2020. A manual analysis of 6-hr sea-level pressure fields identified 153 Arctic cyclones which reached a central pressure less than 984 hPa. The distribution of events is strongly asymmetric about the hemisphere, the vast majority of events occuring

over North America, the North Atlantic, or in the Arctic seas east of Greenland and along coastal Eurasia.

In addition to the distinct hemispheric asymmetry of the prevailing summer-time Arctic storm track, the number of intense, Arctic cyclones varies year-to-year and from month-to-month. For example, August 2015 featured only a single intense Arctic cyclone whereas September of that year featured nine, about 1.5 standard deviations more than the mean. August and September 2016 were particularly remarkable with 7 and 10 intense cyclones, respectively. Interestingly, while late-summer months in 2016 displayed a similar number of events, those cyclones occured in different portions of the Arctic. August 2016 featured cyclones originating over far northeastern Scandinavia and coastal Eurasia, whereas events the following September predominantly formed in the North Atlantic. Evidently the location of the Arctic storm track depends on time of year.

In order to test this hypothesis, August and September months were ranked separately by the number of intense Arctic cyclones. Individual four-month composites were formed over months with the fewest and most intense Arctic cyclones, respectively. These "quiescent" and "stormy" composites were subtracted from one another yielding the difference in upper-level geopotential height anomaly between those periods. It was shown that stormy Augusts are associated with a robust storm track along coastal Eurasia. This is in contrast to stormy Septembers which tend to feature a poleward-oriented (meridional) North Atlantic storm track.

This result explains the relatively rapid transition in the location of the primary Arctic storm track from early August to late September observed in our 2006-2020 climatology. Whereas August, ice-interacting cyclones predominantly form over coastal Eurasia and pass over the Barents, Kara and Laptev Seas, September events primarily develop further west in the North Atlantic and Greenland, Norwegian and Barents Seas. To our knowledge, this is the first intra-seasonal investigation of the development location and tracks of intense Arctic cyclones.

4.2 Synoptic analysis of an intense, ice-interacting Arctic cyclone

As a compliment to the analysis of Mundi (2022), the synoptic-dynamic environment and structural characteristics of an intense cyclone in August 2010 was described during a period of notable sea-ice rearrangement. Development initially occured in a region of cyclonic vorticity advection by the thermal wind over the Greenland Sea. The sea-level pressure lowered, and a cyclonic circulation was established in the lower troposphere. Temperature advection associated with this cyclone subsequently amplified the 1000-500 hPa thickness field. This incipient cyclone continued to develop over the Barents Sea before reaching maturity immediately west of Zemlya Georga.

At this time, an expansive portion of the sea-ice shelf stretching from 0-90E was subject to the cyclone's circulation. This resulted in a dipole in sea-ice concentration changes, off-ice (on-ice) flow associated with daily gains (losses) in sea-ice concentration and a relatively

strong (weak) sea-ice concentration gradient. This signature is ubiquitous among intense Arctic cyclones which near the ice edge and was used to manually filter those events which did and did not interact with sea ice. The expansiveness of such a signal motivates the hypothesis that the primary effect of a summer-time Arctic cyclone on sea ice is to rearrange the local ice shelf.

Of additional interest in this investigation was the affect of cloud radiative effects on the distribution of sea-ice changes. During the post-mature phase of the cyclone life-cycle, a portion of the occluded, thermal ridge structure reached the ice edge. This warm, weakly stratified structure was the primary host of precipitation and featured expansive, deep clouds immediately along an axis of sub-tropical, low potential vorticity air. The reflective effect of this feature towards incoming short-wave radiation was so strong that it entirely off-set the contribution of downward emitted long-wave radiation by the cloud. This resulted in a net negative cloud-radiative effect over a region of pronounced sea-ice concentration losses. Thus, it was concluded that cloud-radiative effects were negligible when compared to the effect of wind and waves.

In order to determine whether the cyclone was associated with a net loss in sea-ice area, changes in sea-ice concentration within a bounded domain were analyzed throughout August 2010. This analysis differs from that of Mundi (2012) in that it uses a larger domain thought to 1) limit the inclusion of open ocean which does not feature sea ice during August 2010 and 2) captures re-arrangement processes by including both sea-ice concentration gains and losses thought to be associated with the cyclonic circulation.

The local sea-ice area decreases dramatically immediately as the cyclone reaches maturity in the Barents Sea. This is coincident with a rapid increase in the magnitude of 6-hr changes in sea-ice area. The magntitude of 6-hr changes in sea-ice area during the storm period were far greater than the regional August 2006-2020 climatology and reached a monthly maxima during the cyclone's mature and post-mature phases. Late in the storm period, however, off-ice flow prevailed in the domain and led to a relatively rapid increase in sea-ice area.

4.3 Recommendations for future work

Given mounting evidence that an effect of intense Arctic cyclones on sea-ice is to reduce the local sea-ice area, it may be hypothesized that periods featuring many intense Arctic cyclones are associated with periods of locally low sea-ice area. A seasonal analysis of the aggregate effect of intense Arctic cyclones on Arctic sea ice would be useful in evaluating this hypothesis. Asymmetry in the summer-time Arctic storm tracks demonstrated in this analysis potentially motivates the evaluation of sea-ice changes in specific regions associated with an active Eurasian or North Atlantic storm track.

One potental problem in any investigation of the interaction of Arctic cyclones with sea-ice is the inherent subjectivity associated with choice of domain. Such decisions, however, can be justified using expert judgement. For example, in this investigation a domain was chosen which was thought to capture the entire storm circulation while simultaneously limiting the inclusion of open ocean. While this empirical analysis is exceedingly useful,

replication of similar analyses for a large collection of storms over larger time periods and spatial domains will present some methodological difficulty.

While in the August 2010 cyclone it appears that cloud-radiative heating was negligible relative to the effect of the cyclone circulation in redistributing ice, this may not be true for all summer-time cases. That said, the strong seasonality in Arctic sunlight hours is consistent with a strong seasonality in the amount of short-wave radiation reflected by clouds associated with Arctic cyclones. During the late-summer this short-wave effect can be quite strong such as to potentially overwhelm the contribution of long-wave radiation by the cloud. In other seasons, however, long-wave radiation emitted downward by the cloud is relatively unabated, potentially producing a net surface warming by radiaiton.

Finally, while the Arctic sea-ice area is of particular interest due to, for example, its role in Arctic albedo, changes in sea-ice area may say relatively little regarding the total sea-ice mass. Further analysis of this cyclone/sea-ice interaction problem would benefit from including discussion regarding local changes in sea-ice thickness. The effect of an individual cyclone on the local sea-ice area may be strongly dependent on ice characteristics like thickness and age. These variables are available at relatively high spatial and temporal resolution and could be incoporated into a case-study analysis similar to that provided here.

Appendix A

Methods for figures in Chapter 1

A.1 Fig. 1.1

Daily observations of sea-ice area were calculated by multiplying the National Snow and Ice Data Center (NSIDC) daily sea-ice concentration (NSIDC-0051, DiGirolamo et al. (2022)) values by the grid area. Observations were first grouped by day of year. Temporal averages and standard deviations were subsequently taken from 1979-2021, 1980-1989 and 2010-2019. This data was plotted from January 1st to December 31st and is presented in Fig. 1.1.

A.2 Fig. 1.2

The NSIDC-0051 sea-ice concentration dataset was grouped by month and averaged from 2006-2020 and 1983-2005, respectively. The 1983-2005 August mean sea-ice concentration

was subsequently subtracted from the 2006-2020 August mean sea-ice concentration in order to demonstrate losses and gains in sea-ice area heading into the first 15 years of the CloudSat/Calipso satellite-era (see Fig. 1.2).

A.3 Fig. 1.3

The NSIDC Ease-Grid sea-ice age, version 4 dataset (NSIDC-0611, Tschudi and CO (2019)) was grouped by year and distributed into the following age groups: 0-1 years, 1-2 years, 3-4 years, and 4+ years. These groups total 100% of the entire ice distribution and were presented in a time-series as a percentage of the total ice distribution (see Fig. 1.3).

A.4 Fig. 1.4

The NSIDC-0051 sea-ice concentration dataset was grouped by month and the August mean and standard deviation was calculated from 2006-2020. These data were presented in Fig. 1.4 as the Augustmean sea-ice variance with the 0.8 sea-ice concentration gradient.

A.5 Fig. 1.5

JRA55 isobaric fields at 1.25° degree spatial and 6-hr temporal resolution were grouped by month and averaged from 1958-2021. The wind speed, Brunt-Vaisala frequency, and temperature gradient were calculated directly from this data. Required derivatives were calculated using 3-point, centered finite differences with 2-point forward and backward differences on the appropriate boundaries. These variables were used to calculate an approximation of the Eady growth rate given by Hoskins and Valdes (1990)

$$\sigma \approx .31 \times \frac{g}{T} |\nabla T| N^{-1}. \tag{A.1}$$

The August mean wind speeds and Eady growth rate was presented at 500 hPa in Fig. 1.5.

Bibliography

Aizawa, T. and H. Tanaka, 2016: Axisymmetric structure of the long lasting summer Arctic cyclones. *Polar Science*, **10**, 192–198, doi:10.1016/j.polar.2016.02.002.

Asplin, M. G., R. Galley, D. G. Barber, and S. Prinsenberg, 2012: Fracture of summer perennial sea ice by ocean swell as a result of Arctic storms: Fracture of perennial sea ice by swells. *J. Geophys. Res.*, **117**, n/a–n/a, doi:10.1029/2011JC007221.

Bjerknes, J. and H. Solberg, 1922: Life cycle of cyclones and the polar front theory of atmospheric circulations. *Geofys. Publ.*, **3**, 1–18.

Blechschmidt, A.-M., A. Richter, J. P. Burrows, L. Kaleschke, K. Strong, N. Theys, M. Weber, X. Zhao, and A. Zien, 2016: An exemplary case of a bromine explosion event linked to cyclone development in the Arctic. *Atmos. Chem. Phys.*, **16**, 1773–1788, doi:10.5194/acp-16-1773-2016.

Boé, J., A. Hall, and X. Qu, 2009: September sea-ice cover in the Arctic Ocean projected to vanish by 2100. *Nature Geosci*, **2**, 341–343, doi:10.1038/ngeo467.

Box, J. E., W. T. Colgan, T. R. Christensen, N. M. Schmidt, M. Lund, F.-J. W. Parmentier, R. Brown, U. S. Bhatt, E. S. Euskirchen, V. E. Romanovsky, J. E. Walsh, J. E. Overland, M. Wang, R. W. Corell, W. N. Meier, B. Wouters, S. Mernild, J. Mård, J. Pawlak, and M. S. Olsen, 2019: Key indicators of Arctic climate change: 1971–2017. *Environ. Res. Lett.*, **14**, 045010, doi:10.1088/1748-9326/aafc1b.

Brummer, B., S. Thiemann, and A. Kirchgabner, 2000: A cyclone statistics for the Arctic based on European Center-analysis data. *Meteorology and Atmospheric Physics*, **75**, 233–250, doi:10.1007/s007030070006.

Cabral, I. S., I. R. Young, and A. Toffoli, 2022: Long-Term and Seasonal Variability of Wind and Wave Extremes in the Arctic Ocean. *Front. Mar. Sci.*, **9**, 802022, doi:10.3389/fmars.2022.802022.

Chang, E. K. M. and I. Orlanski, 1993: On the Dynamics of a Storm Track. *J. Atmos. Sci.*, **50**, 999–1015, doi:10.1175/1520-0469(1993)050¡0999:OTDOAS¿2.0.CO;2.

Charney, J. G., 1947: The dynamics of long waves in a baroclinic westerly current. *J. Meteor.*, **4**, 136–162, doi:10.1175/1520-0469(1947)004¡0136:TDOLWI¿2.0.CO;2.

Clancy, R., C. M. Bitz, E. Blanchard-Wrigglesworth, M. C. McGraw, and S. M. Cavallo, 2022: A cyclone-centered perspective on the drivers of asymmetric patterns in the atmosphere and sea ice during Arctic cyclones. *Journal of Climate*, 1–47, doi:10.1175/JCLI-D-21-0093.1.

DiGirolamo, N., C. Parkinson, D. Cavalieri, P. Gloersen, and H. Zwally, 2022: Sea Ice Concentrations from Nimbus-7 SMMR and DMSP SSM/I-SSMIS Passive Microwave Data.

Eady, E. T., 1949: Long Waves and Cyclone Waves. *Tellus*, **1**, 33–52, doi:10.1111/j.2153-3490.1949.tb01265.x.

Hoskins, B. J. and P. J. Valdes, 1990: On the Existence of Storm-Tracks. *J. Atmos. Sci.*, **47**, 1854–1864, doi:10.1175/1520-0469(1990)047¡1854:OTEOST¿2.0.CO;2.

IPCC, 2022: *The Ocean and Cryosphere in a Changing Climate: Special Report of the Intergovernmental Panel on Climate Change*. Cambridge University Press, first edition.

Kobayashi, S., Y. Ota, Y. Harada, A. Ebita, M. Moriya, H. Onoda, K. Onogi, H. Kamahori, C. Kobayashi, H. Endo, K. Miyaoka, and K. Takahashi, 2015: The JRA-55 Reanalysis: General Specifications and Basic Characteristics. *Journal of the Meteorological Society of Japan*, **93**, 5–48, doi:10.2151/jmsj.2015-001.

Markus, T., J. C. Stroeve, and J. Miller, 2009: Recent changes in Arctic sea ice melt onset, freezeup, and melt season length. *J. Geophys. Res.*, **114**, C12024, doi:10.1029/2009JC005436.

Martin, J. E., 2006: *Mid-Latitude Atmospheric Dynamics: A First Course*. Wiley.

Mundi, C., 2022: Impacts of summer cyclones on arctic sea ice. *Journal of the UW-AOS**, **40**.

Palmén, E. and C. W. Newton, 1969: *Atmospheric Circulation Systems: Their Structure and Physical Interpretation*. Number 13 in International Geophysics Series, Academic Press, New York.

Reitan, C. H., 1974: Frequencies of Cyclones and Cyclogenesis for North America, 1951–1970. *Mon. Wea. Rev.*, **102**, 861–868, doi:10.1175/1520-0493(1974)102¡0861:FOCACF¿2.0.CO;2.

Serreze, M. C. and A. P. Barrett, 2008: The Summer Cyclone Maximum over the Central Arctic Ocean. *Journal of Climate*, **21**, 1048–1065, doi:10.1175/2007JCLI1810.1.

Simmonds, I., C. Burke, and K. Keay, 2008: Arctic Climate Change as Manifest in Cyclone Behavior. *Journal of Climate*, **21**, 5777–5796, doi:10.1175/2008JCLI2366.1.

Simmonds, I. and K. Keay, 2009: Extraordinary September Arctic sea ice reductions and their relationships with storm behavior over 1979–2008. *Geophys. Res. Lett.*, **36**, L19715, doi:10.1029/2009GL039810.

Simmonds, I. and I. Rudeva, 2012: The great Arctic cyclone of August 2012: THE GREAT ARCTIC CYCLONE OF AUGUST 2012. *Geophys. Res. Lett.*, **39**, n/a–n/a, doi:10.1029/2012GL054259.

Stroeve, J., M. M. Holland, W. Meier, T. Scambos, and M. Serreze, 2007: Arctic sea ice decline: Faster than forecast: Arctic ice loss faster than forecast. *Geophys. Res. Lett.*, **34**, doi:10.1029/2007GL029703.

Sutcliffe, R. C., 1947: A contribution to the problem of development. *Q.J Royal Met. Soc.*, **73**, 370–383, doi:10.1002/qj.49707331710.

Tanaka, H., A. Yamagami, and S. Takahashi, 2012: The structure and behavior of the arctic cyclone in summer analyzed by the JRA-25/JCDAS data. *Polar Science*, **6**, 55–69, doi:10.1016/j.polar.2012.03.001.

Trenberth, K. E., 1978: On the Interpretation of the Diagnostic Quasi-Geostrophic Omega Equation. *Mon. Wea. Rev.*, **106**, 131–137, doi:10.1175/1520-0493(1978)106¡0131:OTIOTD¿2.0.CO;2.

Tschudi, M. and U. O. CO, 2019: EASE-Grid Sea Ice Age.

Wang, M. and J. E. Overland, 2009: A sea ice free summer Arctic within 30 years?: ICE-FREE ARCTIC IN 30 YEARS. *Geophys. Res. Lett.*, **36**, n/a–n/a, doi:10.1029/2009GL037820.

Yamagami, A., M. Matsueda, and H. L. Tanaka, 2017: Extreme Arctic cyclone in August 2016: Extreme Arctic cyclone in August 2016. *Atmos. Sci. Lett.*, **18**, 307–314, doi:10.1002/asl.757.

Zhang, J., R. Lindsay, M. Steele, and A. Schweiger, 2008a: What drove the dramatic retreat of arctic sea ice during summer 2007? *Geophys. Res. Lett.*, **35**, L11505, doi:10.1029/2008GL034005.

Zhang, X., J. He, J. Zhang, I. Polyakov, R. Gerdes, J. Inoue, and P. Wu, 2013: Enhanced poleward moisture transport and amplified northern high-latitude wetting trend. *Nature Clim Change*, **3**, 47–51, doi:10.1038/nclimate1631.

Zhang, X., A. Sorteberg, J. Zhang, R. Gerdes, and J. C. Comiso, 2008b: Recent radical shifts of atmospheric circulations and rapid changes in Arctic climate system. *Geophys. Res. Lett.*, **35**, L22701, doi:10.1029/2008GL035607.